Mineralogical Magazine (2023), **87**, 849–865
doi:10.1180/mgm.2023.75

CAMBRIDGE UNIVERSITY PRESS

Article

Secondary uranyl arsenates–phosphates and Sb–Bi-rich minerals of the segnitite–philipsbornite series in the oxidation zone at the Prakovce-Zimná Voda REE–U–Au quartz-vein mineralisation, Western Carpathians, Slovakia

Martin Ondrejka[1], Štefan Ferenc[2], Juraj Majzlan[3], Martin Števko[4,8], Richard Kopáčik[2], Bronislava Voleková[5], Stanislava Milovská[6], Jörg Göttlicher[7], Ralph Steininger[7], Tomáš Mikuš[6], Pavel Uher[1], Adrián Biroň[6], Jiří Sejkora[8] and Alexandra Molnárová[1]

[1]Department of Mineralogy, Petrology and Economic Geology, Faculty of Natural Sciences, Comenius University, Mlynská dolina, Ilkovičova 6, 842 15, Bratislava, Slovakia; [2] Department of Geography and Geology, Faculty of Natural Sciences, Matej Bel University, Tajovského 40, 97401 Banská Bystrica, Slovakia; [3]Institute of Geosciences, Friedrich-Schiller University, Burgweg 11, 07749 Jena, Germany; [4]Earth Science Institute, Slovak Academy of Sciences, Dúbravská cesta 9, 840 05, Bratislava, Slovakia; [5]Slovak National Museum, Natural History Museum, Vajanského nábrežie 2, P.O. BOX 13, 810 06 Bratislava, Slovakia; [6]Earth Science Institute, Slovak Academy of Sciences, Ďumbierska 1, 974 11, Banská Bystrica, Slovakia; [7]Institute for Photon Science and Synchrotron Radiation, Karlsruhe Institute of Technology, Karlsruhe D-76021, Germany; and [8]Department of Mineralogy and Petrology, National Museum, Cirkusová 1740, 193 00 Prague 9, Czech Republic

Abstract

This work is an investigation of the assemblages of supergene minerals occurring in hydrothermal REE–U–Au quartz-vein mineralisation at the Prakovce-Zimná Voda site, Slovakia. Heterogeneous uranyl arsenates and minor phosphates of the autunite group (nováčekite, kahlerite, threadgoldite, autunite, arsenuranospathite and chistyakovaite) together with scorodite and Sb–Bi-rich philipsbornite–segnitite-series minerals formed by oxidising fluids during decomposition and leaching of primary hypogene uraninite, brannerite and base-metal sulfides and sulfosalts. A progressive change of pH from acidic to near-neutral due to the gradual consumption of sulfides resulted in the formation of late phosphuranylite, pharmacosiderite and arseniosiderite. Goethite and other Fe oxides represent the latest hydrous ferric mineral phases and were formed after most of the As was already fixed in Fe arsenates. Antimony and Bi were taken up only into philipsbornite–segnitite and suggest unusual conditions during this process. X-ray absorption spectroscopy indicates that Sb in the philipsbornite–segnitite is fully oxidised (0.1–0.4 apfu Sb^{5+}, octahedral coordination on the *G* site). Pentavalent Sb together with the presence of ferric oxides and arsenates and uranyl minerals suggest oxidative conditions during weathering. This study also indicates that hydrous ferric arsenates are dominant and stable secondary minerals in a supergene environment in a quartz vein rich in Fe and As accompanied by elevated concentrations of U, Pb, Sb, Bi, S, P, Ca and Ba under oxidising conditions.

Keywords: philipsbornite; segnitite; ferric arsenates; ferric oxides; uranyl minerals; weathering; supergene zone; antimony; bismuth; Prakovce-Zimná Voda; Western Carpathians

(Received 16 July 2023; accepted 21 September 2023; Accepted Manuscript published online: 4 October 2023; Associate Editor: G. Diego Gatta)

Introduction

In oxidation zones of uranium deposits, uranyl minerals with autunite-type sheets (known as 'uranium micas') form during the oxidation–hydration weathering of uraninite from acidic solutions which have been generated by the simultaneous oxidative weathering of sulfides (Belova, 1975, 2000; Göb *et al.*, 2013; Krivovichev and Plášil, 2013; Plášil, 2014). Once the sulfides are exhausted, the pH can increase, providing conditions that are conducive for the formation of uranyl minerals with phosphuranylite-type sheets. The mode and results of uraninite–sulfide weathering depend on local parameters, such as mineralogy and geochemistry (e.g. the mass ratio of uraninite to sulfides, or the presence or absence of carbonates) of the ores and the host rocks, their permeability (caused primarily by the rock porosity, or secondarily by the brittle tectonic structures), and the compositional evolution of the percolating ground water (Krivovichev and Plášil, 2013; Plášil, 2014).

Many oxidation zones of uranium and base-metal sulfide deposits, uranium mine tailings, and drainage systems also contain abundant Fe oxides and arsenates. The Fe oxides are typically represented by goethite and ferrihydrite, whereas common crystalline Fe arsenates include scorodite, kaňkite, symplesite, pharmacosiderite, arseniosiderite and yukonite (e.g. Drahota and Filippi, 2009; Lalinská-Voleková *et al.*, 2022).

Corresponding author: Martin Ondrejka; Email: martin.ondrejka@uniba.sk
Cite this article: Ondrejka M., Ferenc Š., Majzlan J., Števko M., Kopáčik R., Voleková B., Milovská S., Göttlicher J., Steininger R., Mikuš T., Uher P., Biroň A., Sejkora J. and Molnárová A. (2023) Secondary uranyl arsenates–phosphates and Sb–Bi-rich minerals of the segnitite–philipsbornite series in the oxidation zone at the Prakovce-Zimná Voda REE–U–Au quartz-vein mineralisation, Western Carpathians, Slovakia. *Mineralogical Magazine* **87**, 849–865. https://doi.org/10.1180/mgm.2023.75

© The Author(s), 2023. Published by Cambridge University Press on behalf of The Mineralogical Society of the United Kingdom and Ireland

https://doi.org/10.1180/mgm.2023.75 Published online by Cambridge University Press

Goethite is stable over a large pH–Eh range and in oxidised conditions, and can precipitate at very low pH if pyrite is oxidised. It commonly contains appreciable amounts of As, which is the most abundant constituent other than Fe^{3+}, followed by Al^{3+}, Si^{4+} and Ca^{2+} (e.g. Göb *et al.*, 2013; Paikaray, 2015; Herrmann *et al.*, 2018). Ferric oxides can adsorb a remarkable amount of As(V) onto their surfaces under neutral and acidic conditions (e.g. Majzlan *et al.*, 2007, 2011; Lalinská-Voleková *et al.*, 2022); their affinity to As(III) is lower than that to As(V) (Cheng *et al.*, 2009).

At low pH and in highly concentrated solutions, scorodite is the most common ferric arsenate secondary mineral formed as a product of oxidation of arsenopyrite or arsenian pyrite. In addition to scorodite, an X-ray amorphous equivalent, termed pitticite, is commonly reported as an important As carrier (Drahota and Filippi, 2009; Das, 2019).

Under near-neutral conditions in the $BaO–CaO–Fe_2O_3–As_2O_5–H_2O$ system, solutions with high As(V) and low Fe(III) concentrations precipitate arseniosiderite and yukonite intimately associated with pharmacosiderite (Paktunc *et al.*, 2015). Several studies have reported the replacement of pharmacosiderite and scorodite by arseniosiderite and its coprecipitation with goethite (Paktunc *et al.*, 2004; Sejkora *et al.*, 2006; Filippi *et al.*, 2007; Drahota *et al.*, 2009). Detailed investigations of localities with secondary ferric arsenates (e.g. Sejkora *et al.*, 2006) show that minerals of the pharmacosiderite supergroup occur at these sites as a minor, generally inconspicuous, phase and that at some localities, pharmacosiderite can be an important, or the dominant, carrier of As (Drahota *et al.*, 2009, Majzlan *et al.*, 2019). Such occurrences seem to be linked to slow weathering under near-neutral conditions. Hence, even at sites where substantial acidity is developed, pharmacosiderite could crystallise in microenvironments that are able to neutralise the acidity (Majzlan *et al.*, 2019). In the presence of Ba, formation of bariopharmacosiderite is favoured and seems to persist even under long-lasting circumneutral conditions (Herrmann *et al.*, 2018).

Supergene processes are also often responsible for the precipitation of alunite-supergroup minerals, for example in base-metal sulfide ore deposits, unconformity-type uranium deposits, pyritiferous rocks, mine drainage, acid soils and saprolite horizons (bauxite, laterite) and confined to the topmost part of the vadose or infiltration zone (Dutrizac and Jambor, 2000; Dill, 2001; Beaufort *et al.*, 2005; Gaboreau *et al.*, 2005, 2007; Welch *et al.*, 2007, 2008, 2009; Adlakha and Hattori 2015). Among alunite-supergroup minerals, the Pb-rich members of the dussertite group, segnitite, ideally $PbFe_3(AsO_{3.5}(OH)_{0.5})_2(OH)_6$ and philipsbornite, ideally $PbAl_3(AsO_{3.5}(OH)_{0.5})_2(OH)_6$ form typically under oxidising and acidic weathering conditions (e.g. Birch *et al.*, 1992; Rattray *et al.*, 1996; Moura *et al.*, 2007; Sejkora *et al.*, 2009, 2011; Mills *et al.*, 2014; Golebiowska *et al.*, 2016; Pekov *et al.*, 2016). The compositional variability of the philipsbornite–segnitite series and the coexistence of several solid solutions among arsenate, phosphate and sulfate alunite-supergroup end-members (notably plumbogummite, hidalgoite, kintoreite and beudantite) accompanied by minor Ba, Cu, Zn, Bi and Sb, has been described from different localities. Examples include Ba-rich philipsbornite from Cínovec, Czech Republic (David *et al.*, 1990), Cu- and Zn-rich beudantite–segnitite-series minerals from Krupka and Jáchymov, Czech Republic (Sejkora *et al.*, 2009, 2011), or Zn-rich segnitite from Broken Hill, Australia (Birch *et al.*, 1992). Furthermore, to date, there have been only a few reported examples of either Bi or Sb, but not both, in alunite-supergroup mineral phases substituting within the octahedral and tetrahedral sites (e.g. Van Wambeke, 1975; Clark *et al.*, 1986; Kolitsch *et al.*, 1999; Mills *et al.*, 2014; Golebiowska *et al.*, 2016; Pekov *et al.*, 2016; Števko *et al.*, 2016; Sejkora *et al.*, 2021).

In this work, we investigated a complex supergene uranyl autunite- and phosphuranylite-group mineral assemblage associated with a variety of supergene Fe arsenates and oxides from the Prakovce-Zimná Voda REE–U–Au quartz-vein mineralisation, Gemeric Unit, Western Carpathians, Slovakia. The aim of this work was a detailed mineralogical study focusing on secondary minerals. In addition, identification of unusual Bi- and Sb-rich minerals of the philipsbornite–segnitite series prompted a detailed crystal chemistry, micro-Raman and X-ray absorption spectroscopy (XAS) investigation to determine compositional variations, substitution mechanisms, valency, and the structural role of Sb and Bi within the investigated members of the dussertite group. Of significant note, the Bi content in the philipsbornite–segnitite series is the highest published Bi_2O_3 content in these minerals and natural samples reported to date.

Uranium occurrences in the Gemeric Unit, Western Carpathians

The Gemeric Unit is the major thick-skinned crustal-scale unit in the Central Western Carpathians, composed of Early Palaeozoic to early Late Carboniferous, mostly low-grade metasediments and metavolcanics intruded by small bodies of Permian granites (Plašienka *et al.*, 1997). Radioactive anomalies and related uranium occurrences in the Gemeric Unit have been a subject of exploration campaigns, prospecting reports, and mineralogical–geochemical research (Varček, 1977; Novotný and Čížek, 1979; Rojkovič and Novotný, 1993; Rojkovič, 1997; Novotný *et al.*, 1999; Donát *et al.*, 2000; Ferenc *et al.*, 2018; Ondrejka *et al.*, 2023a, 2023b). Two principal genetic groups of U mineralisation can be recognised in the Gemeric Unit: (1) stratiform U–Mo deposits and occurrences developed usually in Permian volcano-sedimentary complexes, e.g. Košice (Kurišková-Jahodná), Krompachy (Petrova Hora), Novoveská Huta and Stratená (Rojkovič and Novotný, 1993; Rojkovič, 1997; Kohút *et al.*, 2013) and Cu±U infiltration mineralisation in the copper-bearing Permian sandstones at Novoveská Huta, Šafárka occurrence with uraninite, coffinite, U–Ti oxides, molybdenite, pyrite and chalcopyrite (Ferenc *et al.*, 2022) as primary dominant minerals; and (2) quartz±apatite veins with U–REE±Au and Mo mineralisation, developed in Early Palaeozoic rocks of the Gemeric basement and generally situated in the proximity of the Permian granites, e.g. Betliar, Čučma, Gemerská Poloma (Krátka Dolina), Henclová, Hnilec (Peklisko), and most notably Prakovce-Zimná Voda (Varček, 1977; Rojkovič *et al.*, 1997; Števko *et al.*, 2014; Ferenc *et al.*, 2018; Ondrejka *et al.*, 2023a, 2023b).

Geological setting

The Prakovce-Zimná Voda occurrence is located in the Lower Palaeozoic metamorphic rocks of the Bystrý Potok Formation, a part of the Gelnica Group in the Gemeric Unit (Fig. 1). The metamorphic rocks were intruded by Hummel granites that outcrop 600 m to the south-west of the investigated occurrence. These igneous rocks are leucocratic peraluminous granites with S-type affinity and a relatively high degree of fractionation, evidenced by higher P concentrations in K-feldspar and rare lithophile elements (Li, Rb, Cs, B, Sn, W, Nb and Ta). They originated and

https://doi.org/10.1180/mgm.2023.75 Published online by Cambridge University Press

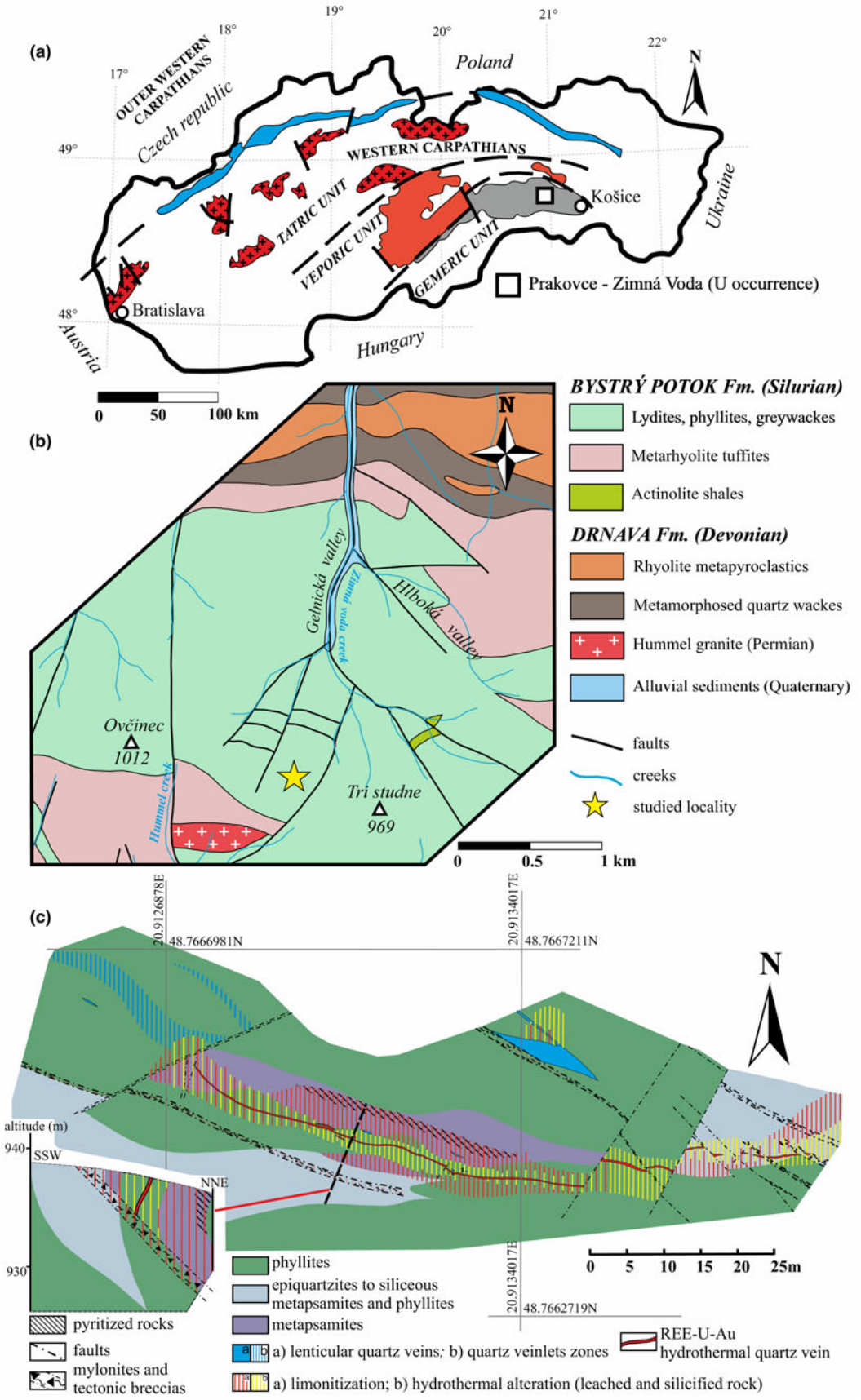

Figure 1. (a) Simplified geological-tectonic sketch-map of the Western Carpathians. (b) A geological map of the area investigated (modified after Bajaník *et al.*, 1984). (c) A close-up view on the veins, alteration and host rocks (modified after Donát *et al.*, 2000; from Ondrejka *et al.*, 2023b, reproduced with permission).

https://doi.org/10.1180/mgm.2023.75 Published online by Cambridge University Press

were emplaced during the post-Variscan, Permian (260–270 Ma) extension (e.g. Villaseñor *et al.*, 2021, and references therein). Moreover, numerous hydrothermal quartz veins with Sb–Au mineralisation occur in the exocontact of the granites (e.g. Zlatá Idka and Poproč deposits near the Prakovce-Zimná Voda occurrence; Kobulský *et al.*, 2011).

Two quartz veins (termed Western and Eastern) with REE–U–Au mineralisation are hosted by fine-grained micaceous phyllites, with interbeds of fine-grained metaquartzites. The Western vein has an E–W strike, total length of ~90 m with an average dip of 65° to the S and conforms to the metamorphic schistosity of the host rocks. The thickness of the vein ranges from 3–30 cm. The vein is slightly corrugated and segmented by transverse faults into 3–55 m long segments, and the termination of the vein on both tails is also tectonic. Drilling surveys showed a tectonic zone cutting the vein at a depth of 7–10 m. The main vein body is accompanied by short veinlets with U–Au mineralisation and quartz veins without ore mineralisation. Along the contact in a zone of 2–8 m thickness, the host rocks are intensively argillitised, locally silicified, and impregnated by pyrite. Supergene alteration of pyritised rocks has caused their limonitisation.

In addition to the dominant quartz, the following hydrothermal minerals have been identified at the Prakovce-Zimná Voda occurrence (Rojkovič *et al.*, 1997; Ondrejka *et al.*, 2023b): uraninite, brannerite, arsenopyrite, pyrite, gold, rutile, bismuth, bismuthinite–stibnite, tintinaite–kobellite, gersdorffite, cobaltite, glaucodot, molybdenite, galena, tetrahedrite-(Fe), fluorapatite, monazite-(Ce), monazite-(Nd), monazite-(Sm), monazite-(Gd), xenotime-(Y), 'xenotime-(Gd)', hingganite-(Y), muscovite, chlorite and members of the tourmaline group. The maximum U content detected in the ore is 11,850 ppm (3080 ppm on average) and the maximum Au content is 164 ppm, with 25 ppm on average (Rojkovič *et al.*, 1997). The REE orthophosphates are exceptionally rich in middle rare earth elements (especially Gd) and precipitated in response to the alteration of the primary uraninite, brannerite and fluorapatite by low-temperature hydrothermal fluids. Further details and description of the uraninite and REE minerals can be found in Ondrejka *et al.* (2023b).

Analytical methods

Electron probe micro-analyses (EPMA) in wavelength-dispersive spectrometry (WDS) mode were performed with a JEOL JXA–8530FE electron microprobe (Earth Science Institute of the Slovak Academy of Sciences, Banská Bystrica, Slovakia) using 15 kV accelerating voltage and 15–20 nA beam current. The beam diameter varied, usually from 3–5 μm. A more focused <1–3 μm beam was used for small heterogeneous domains, however, even this beam size was not adequate for analysis of small domains. The microprobe was calibrated with natural and synthetic standards (Supplementary table S1), and the raw counts (20 s for all elements and 10 s for each background) were converted to wt.% of oxides using the ZAF matrix correction. Elemental contents in the mineral formulae are expressed in atoms per formula unit (apfu). The autunite-type minerals (U–As–P) were calculated based on 12 oxygen atoms. The pharmacosiderite (Pmsd), bariopharmacosiderite (Bpsd) and arseniosiderite (Assd) empirical formulae were normalised on the basis of (P + As + Si + S) = 3 apfu and zeolitic H_2O content was calculated from the nominal formula with $H_2O = 6.5$ (Pmsd), $H_2O = 5$ (Bpsd), $H_2O = 3$ (Assd) and OH, O on ideal stoichiometry. Scorodite (Scd) was calculated on the basis of (P + As + Si + S) = 1 and H_2O content was taken from the nominal formula as $H_2O = 2$. The alunite-supergroup minerals nomenclature used is after Bayliss *et al.* (2010) and the formulae of philipsbornite (Pbn) and segnitite (Sgt) were normalised on the basis of $\Sigma(T + G) = 5$ cations and the total H_2O content calculated assuming OH + F = 7 apfu. All mineral compositional plots were achieved using the *CorelKit* plug-in for *CorelDRAW* (Zhang *et al.*, 2023).

The X-ray absorption near-edge structure (XANES) spectroscopy data were collected at the beamline of the Synchrotron Radiation Laboratory for Environmental Studies (SUL-X, Angströmquelle Karlsruhe, Germany) in the synchrotron radiation source ANKA. A silicon (111) crystal pair with a fixed beam exit was used as a monochromator. The X-ray beam was aligned to an intermediate focus, and then collimated by slits located at the distance of the intermediate focus to ~100 × 100 μm and subsequently focused with a Kirkpatrick-Baez mirror pair to ~50 × 50 μm at the sample position.

The μ-XAS spectra at the SbL_1 and L_3 edges were measured in transmission (standard) and fluorescence (samples) mode in energy steps of 5 eV in the region from −150 to −50 eV relative to the absorption edge, of 2 eV in the region from −50 eV to −20 eV, of 0.5 eV from −20 eV to +20 eV, and with a k step of 0.05 from +20 eV to +400 eV (~k = 10). The intensity of the primary beam was measured by an ionisation chamber. Fluorescence intensities were collected with a seven element Si(Li) solid-state detector with the energy window set to the Sb lines. Data were dead-time corrected, summed for all seven channels and divided by the input intensity, which was measured in an ionisation chamber prior to the sample analysis. The collected data were processed by *ATHENA* (Ravel and Newville, 2005).

The reference compounds used for the determination of the oxidation state and coordination geometry were natural stibnite ($Sb_2^{3+}S_3$), synthetic schafarzikite ($FeSb_2^{3+}O_4$), tripuhyite ($FeSb^{5+}O_4$), Sb(V)-doped fresh ferrihydrite, and Sb^{5+}-doped ferrihydrite aged to goethite.

The Raman spectra were obtained using a Thermo Scientific DXR3xi Raman Imaging microscope at the Slovak National Museum, The Natural History Museum in Bratislava, Slovakia. Several lasers were used during investigation, mainly 785 nm and 633 nm with 100× objective, 25 μm confocal pinhole and an EMCCD detector. The spectra were acquired from approximately the same spots as the EPMA at a laser power of 0.2–10 mW between 0.05 and 2 s (80 scans for a cycle) in ranges of 50–1800 cm^{-1}. The processing of spectra was carried out using the Thermo Fisher Scientific *OMNIC v. 9.11* software package. Spectra of segnitite and philipsbornite were also measured on a LabRAM HR800 spectrometer (Horiba Jobin-Yvon), through an Olympus BX41 microscope confocally coupled to a Czerny-Turner type monochromator (focal length 800 mm). Laser wavelengths of 532 and 633 nm were used for excitation, the Raman-scattered light was collected in 180° geometry through a long-working distance 100×0.8 objective and dispersed by diffraction grating with 600 gr/mm onto a cooled CCD chip. The system resolution was <6 cm^{-1}. The Rayleigh line of excitation and a Teflon standard were used for calibration. The measurement conditions were adjusted to avoid thermal damage of delicate mineral aggregates. Spectra were pre-processed in *Labspec5* software (Horiba Jobin-Yvon) and deconvoluted to single peaks by Gaussian–Lorentzian band shapes in *PeakFit* software version 4.12. The Raman activity of vibrational modes was calculated on the Bilbao crystallographic server (Kroumova *et al.*, 2003) using the crystallographic data for philipsbornite (Cooper and Hawthorne, 2012).

https://doi.org/10.1180/mgm.2023.75 Published online by Cambridge University Press

Powder X-ray diffraction (XRD) analysis was performed using a Bruker D8 Advance diffractometer using Cu$K\alpha$ radiation generated at 40 kV and 40 mA and an energy-dispersive Sol-XE detector. The beam was collimated with a slit assembly of 0.3°-6 mm–0.3°-0.2 mm, with primary and secondary Soller slits at 2.5°. The sample was scanned as random powder using a Si holder from 2 to 65°2θ with step size 0.02°2θ and 3 s counting time. Data were processed with the software *DIFFRAC.EVA* and *PDF2/2010* database.

Results

Sample description and primary ore minerals

The minerals investigated were identified in 16 thin sections and mounts sampled from the REE–U–Au site (Western vein). Primary hypogene minerals, sometimes visible by the unaided eye, occur in fine-grained quartz with abundant stains and veinlets of rusty Fe oxides and arsenates (Fig. 2). Uranium minerals, base-metal sulfides and sulfosalts form clusters irregularly distributed within the vein. Here, macroscopic uraninite is the dominant primary mineral together with abundant brannerite and arsenopyrite accompanied by pyrite, gold, Ni–As–Co–Bi–Pb–Cu sulfides and sulfosalts, especially gersdorffite, galena, minerals of the stibnite–bismuthinite series and tintinaite–kobellite. Hydrothermal phosphates include fluorapatite, monazite- and xenotime-group minerals (Ondrejka *et al.*, 2023a, 2023b).

Supergene minerals

Uranyl arsenates and phosphates

Uranyl arsenates and phosphates represent common secondary products of uraninite and brannerite weathering in the oxidised parts of the REE–U–Au vein mineralisation investigated. They occur as large (<4 mm, mostly 50–150 μm in size) lath-shaped aggregates in close vicinity to altered botryoidal uraninite and arsenopyrite (Fig. 3a–c) or as anhedral clusters in a matrix of ferric oxides, arsenates and quartz (Fig. 3d–e). They also form aggregates (3–4 mm in size) of tabular crystals of yellow–green colour in fissures and cavities of the quartz veins (Fig. 4). These uranyl phases are heterogeneous, with complex substitution mechanisms

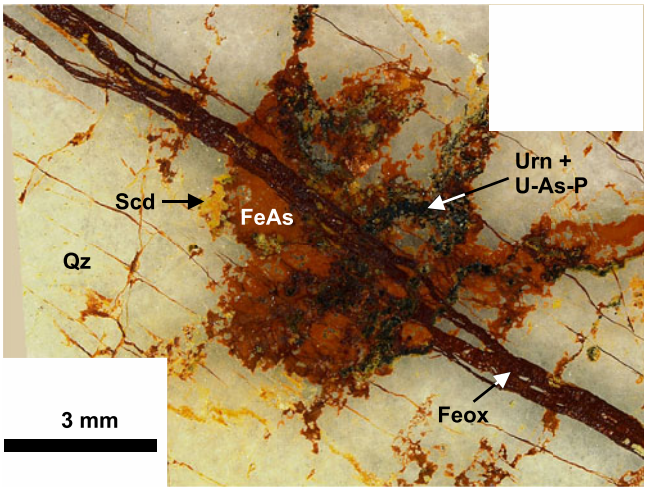

Figure 2. Spatial and cross-cutting relationship of a solitary aggregate of ferric arsenates (FeAs), U minerals and a younger ferric oxide vein (Feox).

within the autunite-type sheet minerals with a general crystal-chemical formula $A^{n+}[(UO_2)(TO_4)](H_2O)_mX_k$. The identified end-members, based on the dominant occupancy of *A* and *T* sites, are predominantly arsenates: (meta)kahlerite $Fe^{2+}(UO_2)_2(AsO_4)_2(H_2O)_{8–12}$; (meta)nováčekite I–II $Mg(UO_2)_2(AsO_4)_2(H_2O)_{8–12}$; and the arsenuranospathite $Al_{1–x}\square_x[(UO_2)(AsO_4)]_2(H_2O)_{20+3x}F_{1–3x}$ to chistyakovaite $Al[(UO_2)(AsO_4)]_2(F,OH)(H_2O)_{6.5}$ series. Less abundant minerals include the uranyl phosphates threadgoldite $Al[(UO_2)(PO_4)]_2(OH)(H_2O)_8$ and autunite $Ca[(UO_2)(PO_4)]_2(H_2O)_{11}$. In addition, minerals with the phosphuranylite-type sheet are represented here by the rare phosphuranylite $CaK(H_3O)_3(UO_2)[(UO_2)_3(PO_4)_2O_2]_2(H_2O)_8$. Phosphuranylite forms pseudomorphs after uraninite in the vein portions where macroscopic sulfides are rare, or completely leached out. It was only identified based on powder XRD data, with the unit-cell parameters: $a = 15.833$ Å, $b = 13.745$ Å, $c = 17.304$ Å and $V = 3766$ Å^3.

The composition and site occupancies of the principal cations in autunite-type minerals are as follows: *T* site = 2.0–24.4 wt.% As_2O_5, 0.16–1.85 apfu As; 0.4–14.0 wt. % P_2O_5, 0.07–1.78 apfu P, which shows the complete substitution of PAs_{-1} (Fig. 5a); and Fe, Mg, or Al as additional cations at the *A* site (≤5.6 wt.% FeO, ≤0.77 apfu Fe; ≤3.9 wt.% MgO, 0.83 apfu Mg; and ≤3.9 wt.% Al_2O_3, 0.6 apfu Al; Fig. 5b). Some measurements also detected Ca as an additional cation (3.5 wt.% CaO, 0.56 apfu Ca; Fig. 5c). The uranyl minerals studied lack monovalent cations, which are common in autunite-group minerals (Fig. 5d). The concentrations of $Na_2O + K_2O$ are below 0.4 wt.%, that of BaO + PbO below 1.5 wt.%, and ZnO + CoO is always less than 0.8 wt.% (Table 1, Supplementary table S2).

Ferric arsenates and oxides

The most abundant ferric arsenates and oxides are scorodite, goethite and pharmacosiderite. The presence of X-ray amorphous iron oxides is very probable; however this was not verified conclusively. Rarer phases include bariopharmacosiderite and arseniosiderite. All minerals were analysed by EPM and the identification of scorodite and goethite was also confirmed by micro-Raman spectroscopy (see Raman spectroscopy section). The ferric arsenates and oxides usually form a fine-grained groundmass and earthy aggregates surrounding the primary ore minerals in quartz–muscovite gangue (Fig. 3a). They also form coatings, pseudomorphs, fissures and cavity fillings, weathering selvages and irregular domains of variable composition around the hypogene ore minerals (Fig. 3b–f), and they are generally rich in Fe, As, Sb, Bi, (Ca, Ba and K) (Fig. 6, Supplementary table S3). Arsenopyrite is partially-or-completely replaced by scorodite, pharmacosiderite + autunite-type arsenates (Fig. 3b–d). The average As content in the ferric oxides is 3.3 wt.%, and the highest content encountered is 10.4 wt.% (Table 1). The Sb content is lower, up to 1.4 wt.% with an average of 0.5 wt.%. Among arsenates, the compositional heterogeneity is controlled by variations in Ca (≤13.7 wt.% CaO, 1.9 apfu Ca in arseniosiderite), Ba, K, Al and P (≤9.9 wt.% BaO, 0.6 apfu Ba; ≤8.2 wt.% K_2O, 1.4 apfu K; ≤7.4 wt.% Al_2O_3, 1.1 apfu Al; and ≤3.4 wt.% P_2O_5, 0.4 apfu P in pharmacosiderite–bariopharmacosiderite), Al and P (≤5.3 wt.% and ≤3.3 wt.% in unspecified arsenates). Homogeneous scorodite shows slightly increased concentrations of P (≤4.6 wt.% P_2O_5, 0.1 apfu P), and Al (≤5.4 wt.% Al_2O_3, 0.2 apfu Al) and thus represents a limited solid solution towards the variscite end-member (Fig. 7, Table 1). The higher totals including calculated H_2O content (>105 wt.%) might be related

https://doi.org/10.1180/mgm.2023.75 Published online by Cambridge University Press

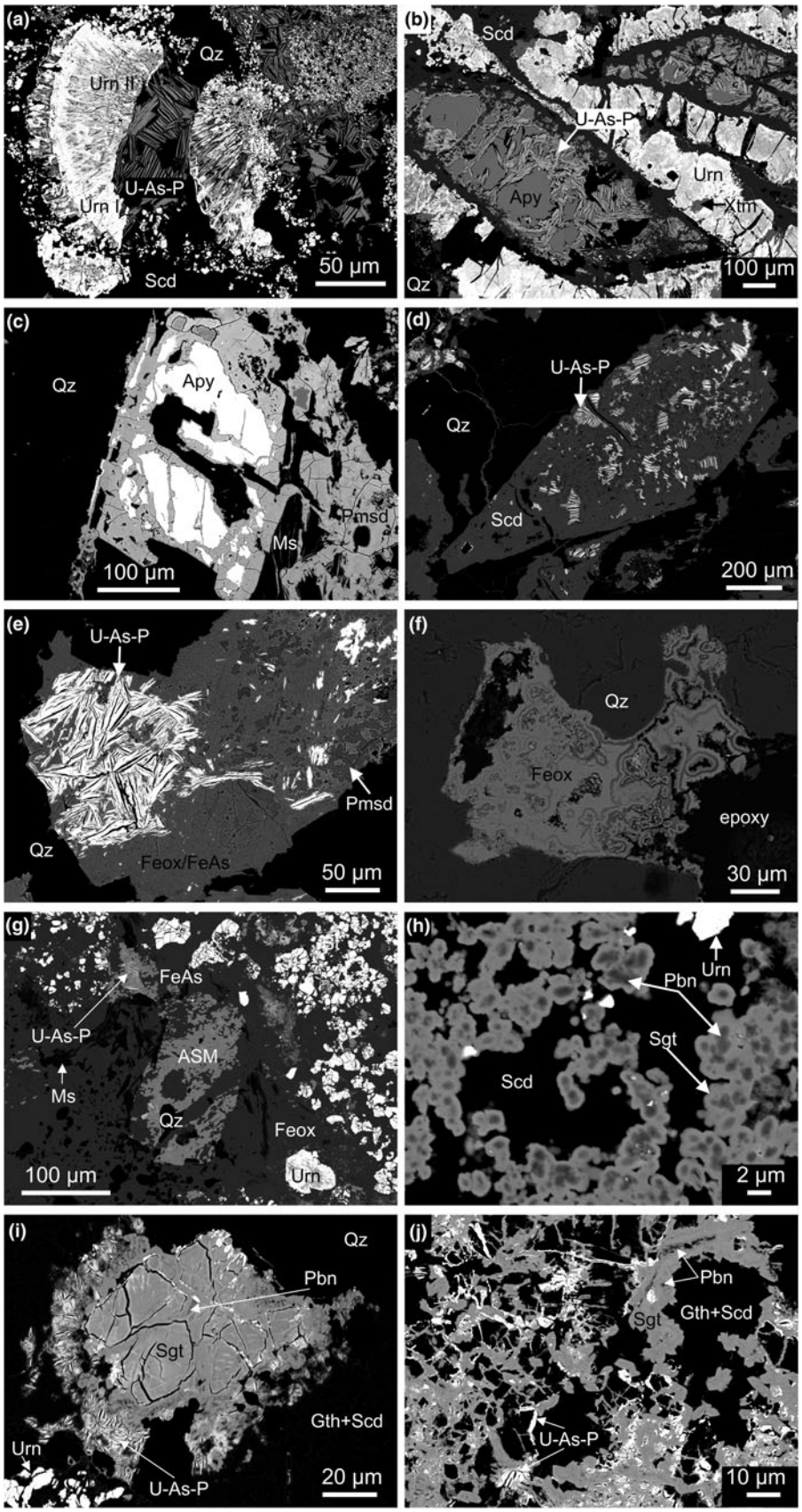

Figure 3. Back-scattered electron images of primary and secondary mineral assemblages from REE–U–Au vein mineralisation at Prakovce-Zimná Voda, Gemeric unit, Western Carpathians, Slovakia. (a) Globular aggregate of uraninite I (Urn I) and its secondary generation consisting of altered rim and inner altered domains (Urn II), associated with secondary uranyl arsenates-phosphates (U–As–P) and quartz (Qz). (b) The ore minerals show signs of decomposition. Arsenopyrite (Apy) and uraninite (Urn) are being replaced by weathering rims of uranyl arsenates-phosphates (U–As–P) and scorodite (Scd). Another mineral is xenotime-(Y) (Xtm). (c) Pharmacosiderite (Pmsd) replacing arsenopyrite (Apy) in quartz (Qz) and muscovite (Ms). (d) Scorodite (Scd) and uranyl arsenates-phosphate (U–As–P) form complete replacement after arsenopyrite(?) in quartz (Qz). (e) Large uranyl arsenates-phosphates cluster (U–As–P) in a heterogeneous aggregate of hydrous ferric oxides/arsenates (Feox/FeAs) and pharmacosiderite (Pmsd) in quartz (Qz). (f) Colloform aggregate of hydrous ferric oxides (Feox) precipitated in the cavity in quartz (Qz). (g) Large aggregate of alunite-supergroup minerals, uraninite (Urn) and uranyl arsenates-phosphates (U–As–P) scattered in fine-grained hydrous ferric oxides (Feox) and hydrous ferric arsenates (FeAs), muscovite (Ms) and quartz (Qz). (h) Alunite-supergroup mineral crystals with colloform banding with concentric zonation rich in philipsbornite (Pbn) in their central parts and segnitite (Sgt) in the outer parts. Other minerals are uraninite (Urn) and scorodite (Scd). (i) Replacement texture of large aggregate of segnitite (Sgt) and tiny relics of philipsbornite (Pbn) rimmed by uranyl arsenates/ phosphates (U–As–P) in iron oxyhydroxide (Gth), scorodite (Scd) and quartz (Qz) groundmass. Another mineral is uraninite (Urn). (j) Replacement texture; the dark relics are philipsbornite (Pbn) and the light colloform and fibrous crystals are segnitite (Sgt) associated with uranyl arsenates/ phosphates (U–As–P) in iron oxyhydroxide (Gth), scorodite (Scd) groundmass. IMA–CNMNC approved mineral symbols according to Warr (2021).

https://doi.org/10.1180/mgm.2023.75 Published online by Cambridge University Press

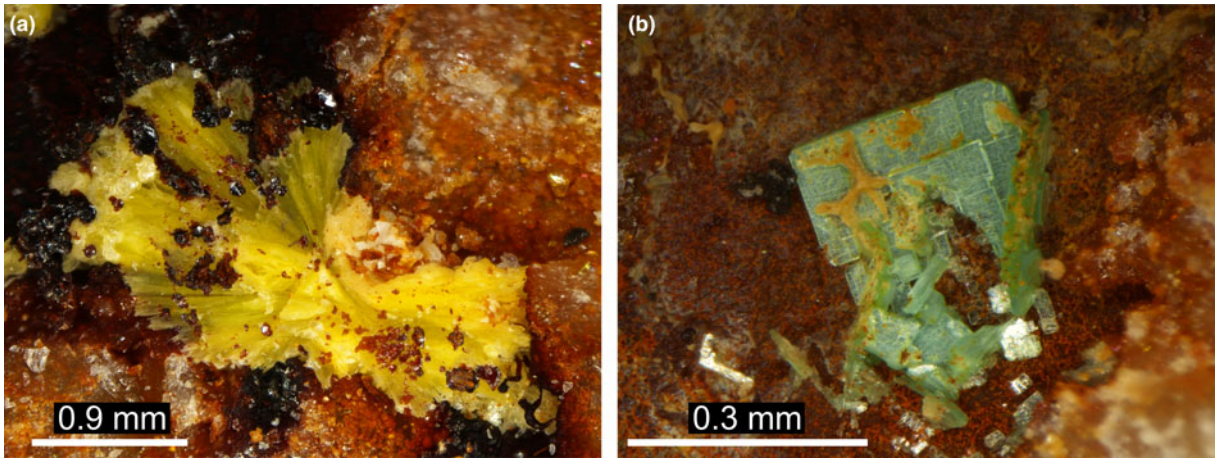

Figure 4. Microphotographs of uranyl arsenates–phosphates. (a) Yellow acicular crystals of arsenuranospathite–chistyakovaite. (b) Well-formed tabular crystal of (meta)nováčekite in a fine-grained rusty mass. Photo Š. Ferenc.

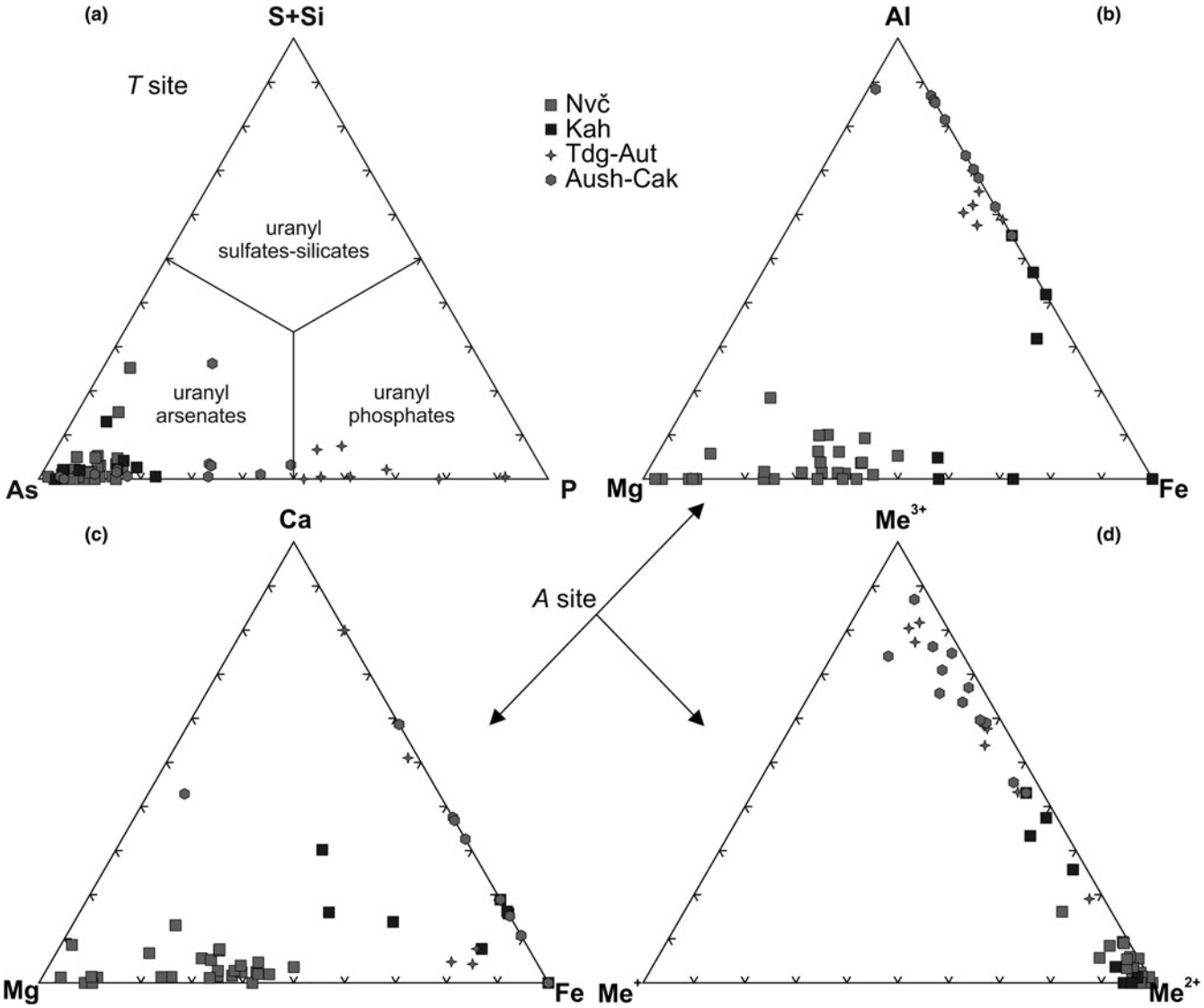

Figure 5. Compositions of uranyl arsenates–phosphates expressed in ternary diagrams (in apfu). Abbreviations are as follows: nováčekite – Nvč, kahlerite – Kah, threadgoldite-autunite – Tdg-Aut, arsenuranospathite-chistyakovaite – Aush-Cak (Warr, 2021).

https://doi.org/10.1180/mgm.2023.75 Published online by Cambridge University Press

to the beam-induced damage during accumulation of the EPMA data rather than the possible occurrence of kaňkite $FeAsO_4{\cdot}3.5H_2O$ (cf. Majzlan *et al.*, 2012).

Composition of alunite-supergroup minerals and speciation of Sb by X-ray absorption spectroscopy

The fine-grained rusty masses consist not only of goethite, scorodite and pharmacosiderite, but also alunite-supergroup minerals. Compositionally, they can be assigned to a mixture of two Pb end-members of the dussertite group: segnitite $[PbFe_3(AsO_{3.5}(OH)_{0.5})_2(OH)_6]$ and philipsbornite $[PbAl_3(AsO_{3.5}(OH)_{0.5})_2(OH)_6]$. They occur as a part of a secondary assemblage in quartz–muscovite gangue or in close vicinity to the secondary uranyl arsenates–phosphates (Fig. 3g). Two distinct intergrowth textures were observed. Most of the alunite-supergroup mineral aggregates show colloform banding with concentric compositional zonation preferentially rich in philipsbornite in their central parts and segnitite in the outer parts (Fig. 3h). In some instances, the replacement texture of subhedral–anhedral microcrystalline aggregates is recognised (Fig. 3i–j).

The alunite-supergroup minerals are compositionally heterogeneous (Table 1, Supplementary table S4), mainly due to the extensive Fe–Al variations and the presence of Sb- and Bi-rich domains. The Fe concentrations on the *G* site range from 9.0 to 27.8 wt.% Fe_2O_3 (0.8–2.3 apfu Fe) and Al ranges from 3.1 to 15.3 wt.% Al_2O_3 (0.5–2.0 apfu Al). There is a strictly core–rim controlled distribution of Al^{3+} by Fe^{3+}, where Al dominates in the core, while Fe dominates in the rim (Fig. 3f and Fig. 8). However, the fine grained character of the segregations of Al-dominant (philipsbornite) and Fe-dominant (segnitite) alunite-supergroup members occasionally prevented reliable analysis of individual minerals. In these cases, the analyses were performed with the beam focused to a small spot, however it is accepted that even this spot was too large to sample a single homogeneous domain. Arsenic is the dominant cation at the *T* site, ranging from 16.5 to 32.0 wt.% As_2O_5 (1.0–1.8 apfu As), though P is elevated in some measurements on philipsbornite (≤10 wt.% P_2O_5; ≤1.0 apfu P) and slightly increased S (≤3.8 wt.% SO_3; ≤0.3 apfu S) suggests only a limited beudantite-group constituent $[PbG_3(As_{0.5}S_{0.5}O_4)_2(OH)_6]$. Though philipsbornite is also rich in the phosphate-dominant plumbogummite-group constituent $[PbG_3(PO_{3.5}(OH)_{0.5})_2(OH)_6]$, the composition of the segnitite rims is close to the ideal arsenate end-member. The alunite-supergroup minerals are anomalously rich in Bi (<10.9 wt.% Bi_2O_3, 0.2 apfu Bi in philipsbornite; ≤9.0 wt.% Bi_2O_3, 0.2 apfu Bi in segnitite) and Sb (≤5.7 wt.% Sb_2O_5, 0.3 apfu Sb in philipsbornite; ≤8.4 wt.% Sb_2O_5, 0.4 apfu Sb in segnitite), in which philipsbornite has an average Bi≈Sb apfu signature whereas segnitite has Sb>Bi apfu. Apart from Bi, the *D* site is occupied almost exclusively by Pb (16.8–29.5 wt.% PbO, 0.5–1.0 apfu Pb) accompanied (Fig. 9) with other minor divalent cations <1.2 wt.% CaO + SrO + BaO (0.1 apfu Ca + Sr + Ba). The concentrations of other trace elements such as Cu, Zn, Th, U, Si and Ce (REE) are negligible and usually below the detection limit (Table 1, Supplementary table S4). The data from EPMA yielded the average empirical formulae: philipsbornite: $(Pb_{0.73}Bi_{0.2}Sr_{0.03}U^{4+}_{0.02}REE^{3+}_{0.01})_{\Sigma 0.99}(Al_{1.6}Fe^{3+}_{1.24}Sb^{5+}_{0.17})_{\Sigma 3.01}(As_{1.15}P_{0.78}S_{0.05}Si_{0.01}O_{3.5}(OH)_{0.5})_{\Sigma 1.99}(OH)_6$, and segnitite: $(Pb_{0.83}Bi_{0.11}Sr_{0.05}U^{4+}_{0.01}REE^{3+}_{0.01})_{\Sigma 1.01}(Fe^{3+}_{1.99}Al_{0.72}Sb^{5+}_{0.3})_{\Sigma 3.01}(As_{1.57}P_{0.4}S_{0.02}O_{3.5}(OH)_{0.5})_{\Sigma 1.99}(OH)_6$.

The oxidation state of antimony in the alunite-supergroup minerals was investigated by μ-XAS. There is a shift of the absorption edge and the crest of the 'white lines' as a function of the oxidation state of Sb at both SbL_1 and SbL_3 edges. The absorption edge of the data set for stibnite is even lower than that for schafarzikite. As the samples contain only antimony bound to oxygen ligands, only oxidic standards were considered further. The XAS 'white line' of the dussertite-type minerals had the same position at different sample spots and overlapped with the 'white lines' of the Sb(V) standards. The difference in the position of the absorption edge (judged from the maxima in the second derivative of the measured curves) is < 0.1 eV (SbL_1 line: Fig. 10). Such a difference lies within the reproducibility of the spectral position for a single sample at the beamline. These data show clearly that all Sb in the samples investigated is in the pentavalent state.

A rudimentary reduction of the EXAFS (extended X-ray absorption fine structure) part of the measured spectra (Supplementary figure S1) leads to similar conclusions. The coordination number of Sb in the samples is close to the coordination number in the tripuhyite standard (6) and much larger than the coordination number of Sb in the schafarzikite standard (3) (Fig. 10).

Raman spectroscopy

The Raman spectra of goethite and As-rich goethite are presented in Fig. 11. The segnitite and philipsbornite spectra (Fig. 12a) show a series of overlapping broad bands in the range of 100–1200 cm^{-1}. Their shapes and positions discriminate these minerals from scorodite. In the segnitite, 11 low frequency bands were resolved. The spectra show a weak broad band in the 545–645 cm^{-1} and 690–1000 cm^{-1} ranges (Fig. 12b). The philipsbornite spectrum in low wavenumbers is characterised by two distinct bands at 140 and 207 cm^{-1} with shoulders and by a broad band in the range of 250–350 cm^{-1}. A series of bands in the region between 390 and 520 cm^{-1} and a broad low intensity structure at 550–620 cm^{-1} were also discerned (Fig. 12a).

Discussion

Compositional variations of philipsbornite–segnitite series

The philipsbornite–segnitite series in the investigated mineralisation represents a heterogeneous and multicomponent solid-solution system. These minerals have wide compositional variations of substantial elements at different crystallographic sites, particularly As–P±S (*T* site), Fe^{3+}–Al^{3+}–Sb^{5+} (*G* site) and Pb–Bi ±(Sr+Ba+Ca) (*D* site). The chemical exchange of this complex solid-solution system is controlled by homovalent and heterovalent substitution mechanisms, documented previously by Van Wambeke (1975), Clark *et al.* (1986), Kolitsch *et al.* (1999), Mills *et al.* (2014), Golebiowska *et al.* (2016) and Pekov *et al.* 2016). The concentric compositional zonation of philipsbornite cores enclosed in segnitite envelopes resulted from early crystallisation of Al-dominant and phosphate-rich alunite-supergroup minerals and late crystallisation of Fe-dominant and arsenate-rich alunite-supergroup minerals, rather than from solid-state diffusion segregation (cf. Desborough *et al.*, 2010). It is obvious that the zoning in the intermediate members is due to the strong coupling of $(AsO_4)^{3-}$ with Fe^{3+} and $(PO_4)^{3-}$ with Al^{3+} (cf. Rattray *et al.*, 1996). The As–Fe and P–Al affinity and the compositional trend from As + Fe towards P + Al is also clearly

https://doi.org/10.1180/mgm.2023.75 Published online by Cambridge University Press

https://doi.org/10.1180/mgm.2023.75 Published online by Cambridge University Press

Table 1. Representative compositions (wt.%) from EPMA of uranyl arsenates and phosphates.*

Wt.%	Kah	Nvč	Aush-Cak	Thr	Aut	Wt.%	Sgt	Sgt	Pbn	Pbn	Wt.%	Scd	Pmsd	Bpsd	Assd	Wt.%	FeAs	Feox	Feox	Feox
SO_3	0.03	0.03	0.01	0.06	0.01	SO_3	0.28	0.20	1.09	0.213	SO_3	0.36	–	0.01	0.02	SO_3	0.03	0.02	0.37	0.02
UO_3	60.09	53.38	61.61	62.77	65.22	P_2O_5	3.17	3.78	7.46	9.993	P_2O_5	0.61	0.93	1.32	0.30	P_2O_5	1.25	0.60	0.23	1.06
P_2O_5	0.42	1.35	0.68	14.04	11.97	As_2O_5	23.97	24.47	19.01	16.5	As_2O_5	51.32	37.51	37.15	43.98	As_2O_5	26.26	15.89	3.37	2.35
As_2O_5	19.03	22.18	20.74	2.01	5.32	Sb_2O_5	8.4	5.52	3.52	3.708	Sb_2O_5	0.08	n.a.	0.01	–	Sb_2O_5	0.29	0.09	1.91	0.26
SiO_2	–	0.14	–	–	–	SiO_2	0.02	–	0.04	0.129	SiO_2	0.08	0.06	0.12	0.32	SiO_2	10.31	0.16	1.75	3.17
Bi_2O_3	–	–	–	–	–	UO_2	0.36	0.37	1.00	1.39	UO_2	0.16	n.a.	0.02	0.20	UO_2	0.16	0.06	12.52	0.33
Al_2O_3	0.02	0.50	2.99	2.53	1.16	Bi_2O_3	1.02	6.34	10.87	6.86	Bi_2O_3	0.04	n.a.	–	0.02	Bi_2O_3	0.01	–	3.22	0.11
Y_2O_3	–	0.04	n.a.	n.a.	n.a.	Fe_2O_3tot	20.16	22.44	10.64	13.13	Fe_2O_3tot	34.47	36.45	32.77	31.80	Fe_2O_3	41.39	78.17	75.44	76.74
La_2O_3	–	–	n.a.	n.a.	n.a.	Al_2O_3	4.41	4.69	16.25	13.28	Al_2O_3	0.66	2.80	5.70	0.15	Al_2O_3	5.48	0.92	0.67	0.35
Ce_2O_3	0.06	–	n.a.	n.a.	n.a.	Ce_2O_3	n.a.	0.05	0.24	0.27	MgO	0.10	–	0.04	–	MgO	0.60	0.01	0.03	–
FeOtot	2.82	3.09	1.91	1.82	1.13	CaO	–	–	–	–	CaO	–	0.03	–	13.50	ZnO	0.15	0.11	–	–
MgO	–	2.29	–	0.04	–	SrO	0.82	–	0.30	0.48	SrO	–	0.10	–	–	CuO	0.05	–	–	0.08
CaO	–	0.14	0.35	1.55	3.52	BaO	–	–	–	–	BaO	0.07	3.55	9.35	0.06	CaO	0.77	0.65	0.01	0.08
SrO	–	0.05	0.04	0.38	1.33	ZnO	–	–	0.03	–	ZnO	0.06	–	0.15	0.07	SrO	0.04	–	–	–
BaO	–	–	–	–	–	CuO	–	–	–	0.02	CuO	0.06	0.02	0.04	0.04	BaO	0.07	1.57	0.18	0.06
CoO	–	0.10	0.03	0.01	–	PbO	29.11	23.86	20.44	24.18	PbO	0.12	–	0.06	0.14	PbO	0.28	0.24	0.50	0.01
ZnO	0.11	0.12	0.23	0.16	–	Na_2O	–	–	n.a.	n.a.	Na_2O	–	0.07	0.06	0.14	Na_2O	0.10	0.18	–	0.02
CuO	2.96	–	0.04	0.07	0.07	K_2O	–	–	n.a.	n.a.	K_2O	0.02	1.82	0.25	–	K_2O	1.18	0.07	0.01	–
PbO	–	–	–	–	–	H_2Ocalc	8.17	8.52	9.07	9.30	H_2Ocalc	16.63	17.38	14.46	7.07	Total	88.41	98.73	100.22	84.64
Na_2O	–	–	–	0.03	0.01	Total	99.88	100.24	99.95		Total	104.83	100.73	101.51	97.81					
K_2O	0.08	0.25	0.15	0.23	0.16															
H_2Ocalc	16.00	17.51	13.73	18.75	14.66															
Total	101.61	101.15	102.53	104.46	104.56															

Apfu	Kah	Nvč	Aush-Cak	Thr	Aut	Apfu	Sgt	Sgt	Pbn	Pbn	Apfu	Scd	Pmsd	Bpsd	Assd	Wt.%	FeAs	Feox	Feox	Feox
S^{6+}	0.004	0.003	0.002	0.007	0.001	S^{6+}	0.027	0.018	0.095	0.018	S^{6+}	0.010		0.001	0.002	S^{6+}	0.014	0.01	0.15	0.01
P^{5+}	0.062	0.187	0.092	1.775	1.499	P^{5+}	0.345	0.394	0.730	0.955	P^{5+}	0.019	0.115	0.162	0.032	P^{5+}	0.544	0.26	0.10	0.46
As^{5+}	1.743	1.900	1.735	0.157	0.411	As^{5+}	1.609	1.576	1.150	0.974	As^{5+}	0.968	2.876	2.819	2.925	As^{5+}	17.122	10.36	2.20	1.53
Si^{4+}		0.024	0.001			Si^{4+}	0.002		0.004	0.015	Sb^{5+}	0.001	-	0.002		Sb^{5+}	0.215	0.07	1.44	0.20
ΣX	1.810	2.114	1.829	1.939	1.911	ΣT	1.984	1.988	1.980	1.961	Si^{4+}	0.003	0.009	0.018	0.040	Si^{4+}	4.817	0.08	0.82	1.48
U^{6+}	2.210	1.835	2.068	1.968	2.025	Sb^{5+}	0.401	0.252	0.152	0.155	U^{4+}	0.001		0.001	0.006	U^{4+}	0.140	0.05	11.03	0.29
Bi^{3+}						Fe^{3+}	1.948	0.680	1.415	1.767	Fe^{3+}	0.936	4.022	3.579	3.044	Bi^{3+}	0.009	–	2.89	0.10
Al^{3+}	0.003	0.097	0.563	0.446	0.202	Al^{3+}	0.667	2.079	1.451	1.115	Al^{3+}	0.028	0.484	0.975	0.022	Fe^{3+}	28.946	54.67	52.76	53.67
Y^{3+}		0.003	-	-	-	Cu^{2+}				0.002	Bi^{3+}				0.001	Al^{3+}	2.902	0.48	0.36	0.19
La^{3+}			-	-	-	Zn^{2+}			0.003		Mg^{2+}	0.003		0.005		Mg^{2+}	0.205	–	0.01	–
Ce^{3+}	0.004		-	-	-	ΣG	3.016	3.012	3.020	3.039	Zn^{2+}	0.001		0.016	0.006	Zn^{2+}	0.117	0.09	–	–
Fe^{2}	0.413	0.423	0.256	0.228	0.140	U^{4+}	0.010	0.010	0.026	0.035	Cu^{2+}	0.002	0.002	0.004	0.004	Cu^{2+}	0.042	–	–	0.06
Mg^{2+}		0.559		0.009		Bi^{3+}	0.034	0.201	0.324	0.200	Ca^{2+}		0.005		1.840	Ca^{2+}	0.547	0.46	0.01	0.06
Ca^{2+}		0.024	0.061	0.248	0.558	Ce^{3+}	-	0.002	0.010	0.011	Sr^{2+}		0.008			Sr^{2+}	0.037	–	–	–
Sr^{2+}		0.005	0.004	0.033	0.114	Ca^{2+}					Ba^{2+}	0.001	0.204	0.532	0.003	Ba^{2+}	0.064	1.40	0.16	0.05
Ba^{2+}						Sr^{2+}	0.061	0.043	0.020	0.031	Pb^{2+}	0.001		0.002	0.005	Pb^{2+}	0.260	0.22	0.46	0.01
Co^{2+}		0.014	0.003	0.001		Ba^{2+}					Na^{+}		0.340	0.016	0.034	Na^{+}	0.074	0.13	–	0.02
Zn^{2+}	0.014	0.015	0.028	0.018		Pb^{2+}	1.006	0.791	0.637	0.735	K^{+}	0.001	0.021	0.046		K^{+}	0.977	0.06	–	–
Cu^{2+}	0.392		0.005	0.008	0.008	Na^{+}				-	Total	1.974	8.088	8.178	7.965	Total	57.032	68.36	72.40	58.13
Pb^{2+}						K^{+}				-										
Na^{+}				0.008	0.004	ΣD	1.111	1.048	1.017	1.011										
K^{+}	0.018	0.052	0.031	0.043	0.031	Total	6.111	6.048	6.017	6.011										
ΣA	3.054	3.027	3.019	3.010	3.082															
Total	4.864	5.141	4.848	4.949	4.993															

*Abbreviations: kahlerite – Kah; nováčekite – Nvč; arsenuranospathite–chistyakovaite – Aush–Cak; threadgoldite – Tdg; autunite – Aut; segnitite (Sgt); philipsbornite (Pbn). Ferric arsenates: scorodite – Scd; pharmacosiderite – Pmsd; bariopharmacosiderite – Bpsd; arseniosiderite – Assd. Unspecified arsenates – FeAs; Ferric oxide – Feox.
n.a. – not analysed; '–' below detection.

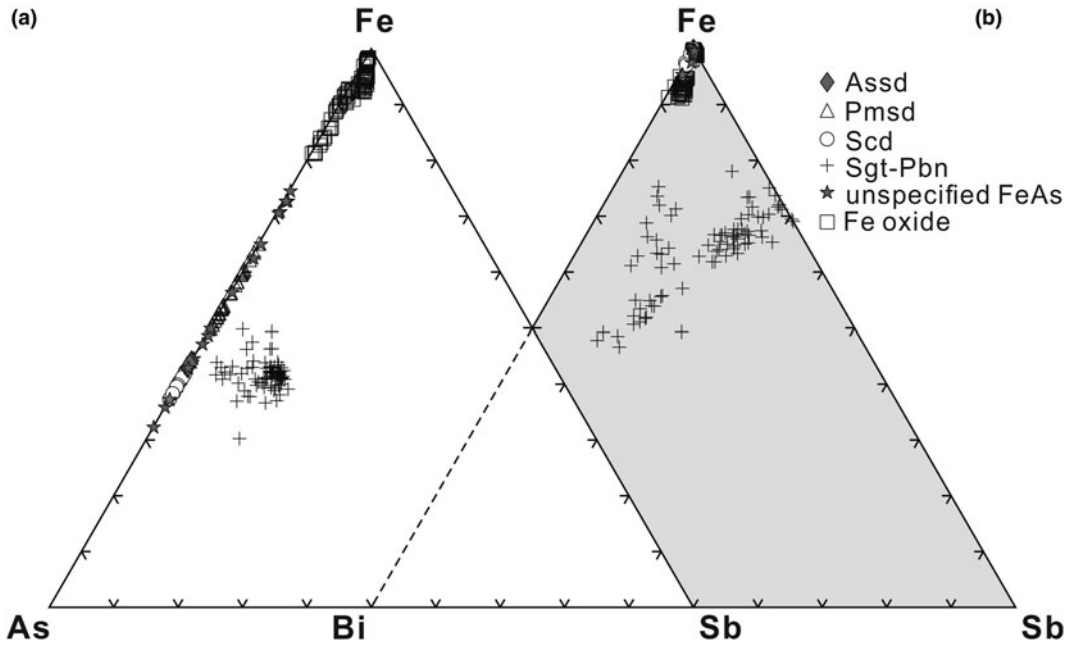

Figure 6. Compositions of the supergene mineral assemblage in: (a) Fe–As–Sb ternary diagram; and (b) Fe–Bi–Sb ternary diagram (in atomic wt.%). Abbreviations are: arseniosiderite – Assd, pharmacosiderite – Pmsd, scorodite – Scd, segnitite-philipsbornite – Sgt-Pbn (Warr, 2021).

recognised in other Fe arsenates (scorodite, pharmacosiderite and only slightly in arseniosiderite) (Fig. 7). This geochemical and spatial strong association and synergy is well documented especially for As and Fe in weathering products (e.g. Walker *et al.*, 2005; Lalinská-Voleková *et al.*, 2012). The compositional gap between Al and Fe^{3+} in the philipsbornite–segnitite series (Sejkora *et al.*, 2011; Golebiowska *et al.*, 2016) is not observed in our samples. We have to admit, though, that the cause therefore may lie in the fact that the beam size for the EPMA exceeded the small size of the domains in these minerals.

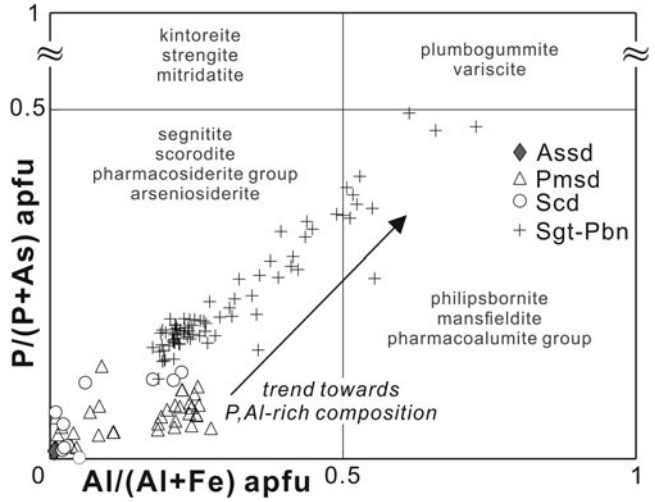

Figure 7. Composition of supergene minerals in an Al/(Al + Fe) vs P/(P + As) compositional diagram. The selection of alunite-supergroup minerals end-members containing P + As in the *T* site is restricted to Pb-dominant end-members of the dussertite and plumbogummite groups, the variscite group excluding yanomamite, Fe–Al members of pharmacosiderite group and mitridatite group containing Ca–Fe-dominant end-members (atomic proportions).

The minor constituents of particular interest in the alunite-supergroup minerals are Sb and Bi. In supergene environments, Sb is expected to be found in its highest, pentavalent oxidation state. We assume that the alunite-supergroup minerals studied formed in such an environment by weathering of the primary base-metal mineralisation at Prakovce-Zimná Voda. This assumption agrees well with the results of the XAS which shows only Sb^{5+} in our samples (Fig. 10). Similarly, μ-EXAFS and XANES data of Sb-rich segnitite from Black Pine mine in Montana, USA suggested that Sb is present as Sb^{5+} (Mills *et al.*, 2014). However, the associated EPMA in Mills *et al.* (2014) did not include data for P and Si but show a systematic deficiency at the *T* site (1.75–1.87 apfu As). Mills *et al.* (2014) rationalised this deficiency by an alternative fit to the XAS data with 85% Sb^{5+} and 15% Sb^{3+}. Using their EXAFS data, they determined the octahedral coordination of Sb^{5+} and tetrahedral coordination of Sb^{3+}. Doing so, they assigned Sb^{3+} to the *T* site, even though tetrahedral coordination of Sb^{3+} is highly unlikely because of its need to position the lone electron pair in its coordination environment. A small part of Sb^{3+} at the *T* site is also conceded in aliovalent Sb-rich segnitite from Berezovskoe gold deposit, Middle Urals, Russia (Pekov *et al.*, 2016). The EPMA data from our samples do not show a significantly deficient *T* site (average occupancy of 2.0 apfu; Table 1) and all Sb here is considered to be pentavalent in octahedral coordination on the *G* site (0.1–0.4 apfu Sb^{5+}), as previously reported in 'antimonian' dussertite from the Clara mine, Germany (cf. Kolitsch *et al.*, 1999). The substantial content of pentavalent cations on the *G* site and the exchange of $(Al,Fe)^{3+}$ for Sb^{5+} requires compensation by the deprotonation of oxygen atoms in the (AsO_3OH) tetrahedra *via* the $0.5Sb^{5+} + (AsO_4)^{3-} \leftrightarrow 0.5Fe^{3+} + (AsO_3OH)^{2-}$ substitution mechanism (Kolitsch *et al.*, 1999; Pekov *et al.*, 2016).

Furthermore, Bi in alunite-supergroup minerals occurs rarely and there are only two known Bi-dominant end-members:

https://doi.org/10.1180/mgm.2023.75 Published online by Cambridge University Press

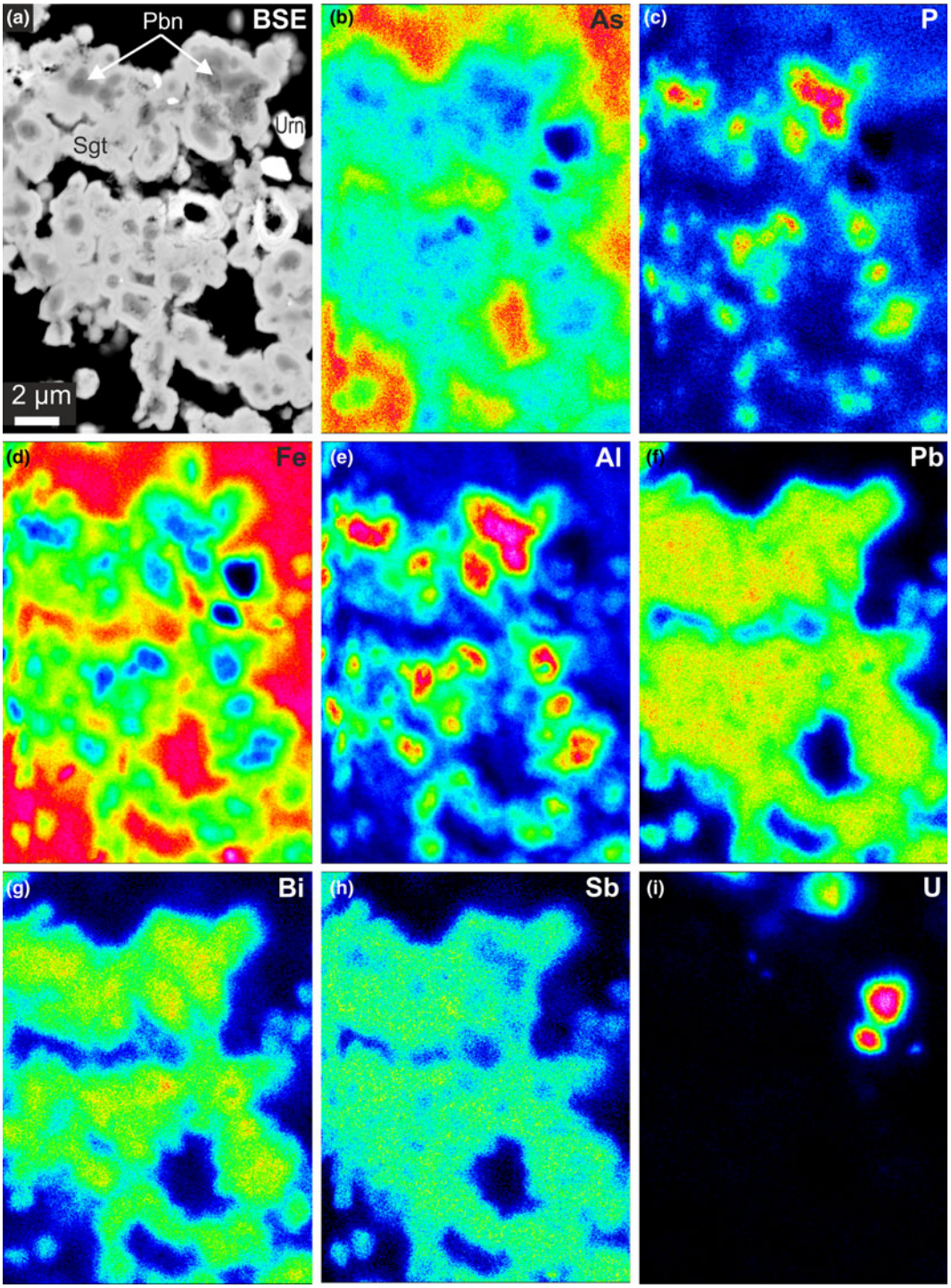

Figure 8. False colour X-ray map showing the distribution of selected elements in the aggregate of a philipsbornite–segnitite series mineral.

waylandite $BiAl_3(PO_4)_2(OH)_6$ (von Knorring and Mrose, 1963; Clark *et al.*, 1986; Mills *et al.*, 2010; Uehara and Shirose, 2013); and zaïrite, $BiFe_3(PO_4)_2(OH)_6$ (Van Wambeke, 1975). The arsenate-analogue of waylandite is described incompletely by Scharm *et al.* (1994) as 'arsenowaylandite' and is questionable because of inadequate data. Of these Bi-dominant alunite-supergroup mineral phases, only waylandite occurs at more than one locality. The significant Bi content in dussertite, beudantite and plumbogummite groups in the alunite supergroup has been described rarely, e.g. from a supergene zone in the Ľubietová, Podlipa deposit, Slovakia, ≤7.85 wt.% Bi_2O_3, 0.3 apfu Bi (Števko *et al.*, 2016) and from the oxidation zone of the Berezovskoe gold deposit, Middle Urals, Russia ≤0.5 wt.% Bi_2O_3, 0.02 apfu Bi (Pekov *et al.*, 2016). Regarding their Bi content, our samples (<10.9 wt.% Bi_2O_3; 0.3 apfu Bi) represent intermediate compositions between philipsbornite–plumbogummite–segnitite and their hypothetical 'arsenowaylandite'–waylandite–'arsenozaïrite' end-members.

https://doi.org/10.1180/mgm.2023.75 Published online by Cambridge University Press

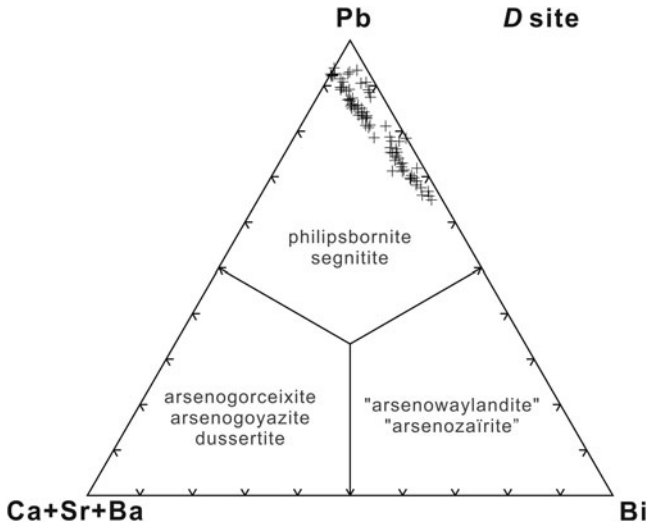

Figure 9. Composition of alunite-supergroup minerals showing *D*-site occupancy in a Pb–(Sr+Ba+Ca)–Bi ternary diagram. (in atomic wt.%).

Raman spectroscopic identification of minerals and implications

The Raman spectra of goethite agree well with those published previously (e.g. De Faria *et al.*, 1997; Das and Hendry, 2011). The spectra of As-rich goethite are characteristic by the presence of a band at 804–807 cm^{-1}, which can be assigned to the symmetric stretching vibration of the arsenate anion (Müller *et al.*, 2010; Kloprogge and Wood, 2017). The band is strong for samples of goethite with high As content (5.4–12.9 wt.%) and is not visible when the As content is lower than 3.5 wt.% (see Fig. 11).

The Raman spectra of segnitite and philipsbornite show broad peaks in the range of 850–900 cm^{-1} however these are missing in our (and published) scorodite data (Myneni *et al.*, 1998; Filippi *et al.*, 2007; Culka *et al.*, 2016). Our spectra of segnitite and philipsbornite are almost identical and only deconvolution revealed minor differences, as could be expected from their structural and chemical similarity within the dussertite group. The philipsbornite spectra also agree well with the RRUFF database (R060683, Lafuente *et al.*, 2015). That, however, is contradictory to a difference found in the spectrum of philipsbornite in Frost *et al.* (2013). As these authors provide the only interpretation published to date, we adopted their peak assignment of segnitite and applied it to both segnitite and philipsbornite, relying on the accuracy of our and RRUFF records (see Fig. 12). The segnitite band centred at 863 cm^{-1} is due to ν_1 symmetric stretching vibrations of $(AsO_4)^{3-}$ and 807 cm^{-1} is attributed to $(AsO_4)^{3-}$ ν_3 antisymmetric stretching (Frost *et al.*, 2005). In dussertite, peaks near 700 and 750 cm^{-1} are related to the As–OH stretching mode (Frost *et al.*, 2011), possibly analogous to bands at 699 and 756 cm^{-1} in our segnitite spectra. The 320–500 cm^{-1} wavenumber range contains bands assigned to ν_2 and ν_4 $(AsO_4)^{3-}$ ion-bending modes. The philipsbornite broad band at 856 cm^{-1} can be assigned to ν_1 symmetric stretching of $(AsO_4)^{3-}$, the bands at 696 and 753 cm^{-1} to As–OH stretching mode. The series of bands in the range of 370–550 cm^{-1} belong to bending modes ν_2 and ν_4 within the $(AsO_4)^{3-}$ ion. According to Frost *et al.* (2013) symmetric stretching vibrations might overlap with antisymmetric bands. The multiple overlapping bands indicate loss of degeneration due to strong distortion of the $(AsO_4)^{3-}$ tetrahedra which might be enhanced by substitutions in both cation and anion positions. The peaks of lower intensity centred at 945 and 941 cm^{-1} are assigned to symmetric stretching modes of $(PO_4)^{2-}$ and the peak at 991 cm^{-1} in segnitite to analogical modes of $(SO_4)^{2-}$ units. This suggests a mixed composition of measured phases within the philipsbornite–segnitite series. Our calculation of vibrational Raman activity on the base of group theory shows that the cation bonding in octahedral position (9d Wyckoff position) should not be observed in Raman spectra.

Evolution of the oxidation zone and formation of supergene minerals

Mineralogical and textural observations suggest that the oxidation zone evolved through several stages (Fig. 13):
(I) Oxidation–hydration weathering of uraninite. The primary uraninite I was converted to uraninite II and 'gummite' under near-neutral conditions. Texturally, this stage is marked by an increase of porosity and fracturing. The products of this stage have been described in more detail by Ondrejka *et al.* (2023b).
(II) Initial acidic stage. Massive oxidation of sulfides modified and buffered the composition of the weathering fluids. Here, the sulfide oxidation led to an increased activity of H^+, formation of acid-rock drainage, and attack of the pre-existing uraninite, brannerite, fluorapatite and muscovite. The acidic solutions were supplied with arsenate, phosphate, sulfate, uranyl, Fe(III), Al(III), Pb(II), Sb(V), As(V), Bi(III), and other elements released into the solution. This stage is characterised by the formation of diverse autunite-type minerals (kahlerite, nováčekite, arsenuranospathite,

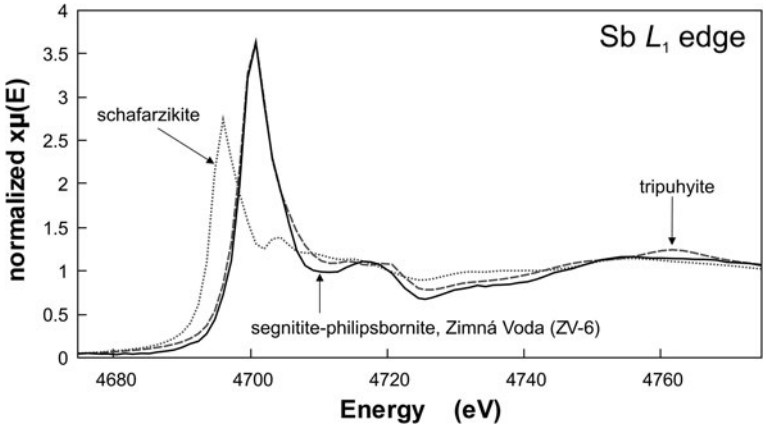

Figure 10. Comparison of the data for sample ZV-6 with the reference Sb(III) and Sb(V) compounds in the XANES region of the SbL_1 edge.

https://doi.org/10.1180/mgm.2023.75 Published online by Cambridge University Press

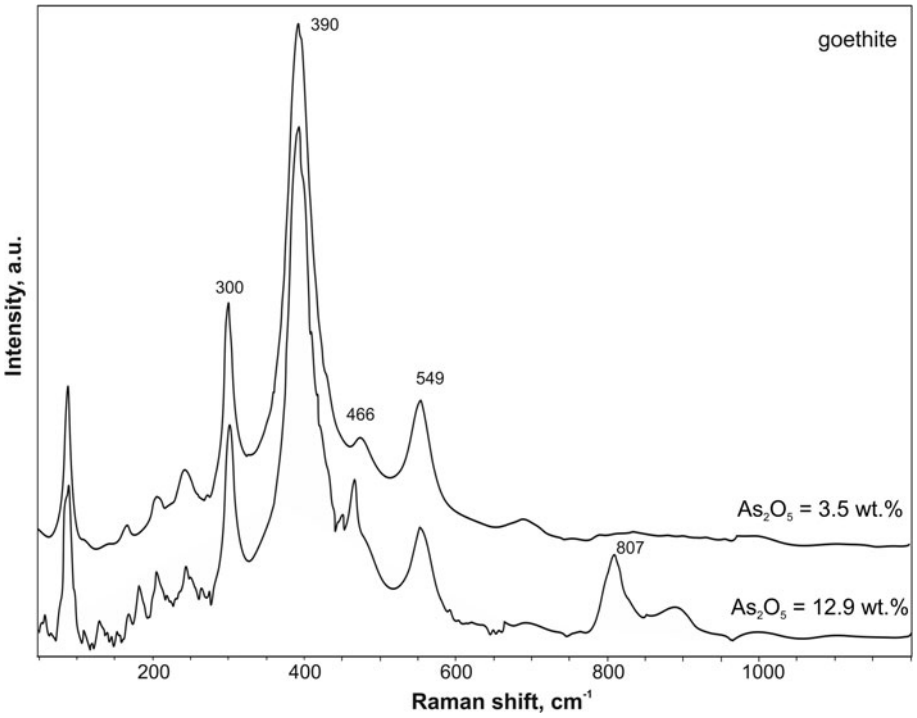

Figure 11. Untreated Raman spectra of goethite excited by a 785 nm laser.

chistyakovaite, threadgoldite and autunite) accompanied by abundant scorodite, hydrous ferric arsenates and locally abundant philipsbornite–segnitite-series minerals that represent the sole sink of the remobilised Sb and Bi.

(III) Advanced acidic-neutral stage. Phosphuranylite forms as a direct replacement of uraninite in the vein portions without sulfide remnants. Both arsenopyrite and scorodite are replaced by pharmacosiderite and later bariopharmacosiderite and arseniosiderite. These minerals precipitate under near-neutral conditions, after the acidity-generating capacity of the sulfides has been exhausted.

(IV) Mature stage. The latest goethite and other Fe oxides form after most of the As was already fixed in Fe arsenates. The Fe oxides form the youngest veinlets that crosscut the older supergene minerals or replace pharmacosiderite.

Fate and uptake of Sb and Bi in the oxidation zone

The main carriers of Sb and Bi in the oxidation zone are surprisingly the arsenates of the philipsbornite–segnitite series. Other supergene minerals, particularly Fe oxides that are usually eager

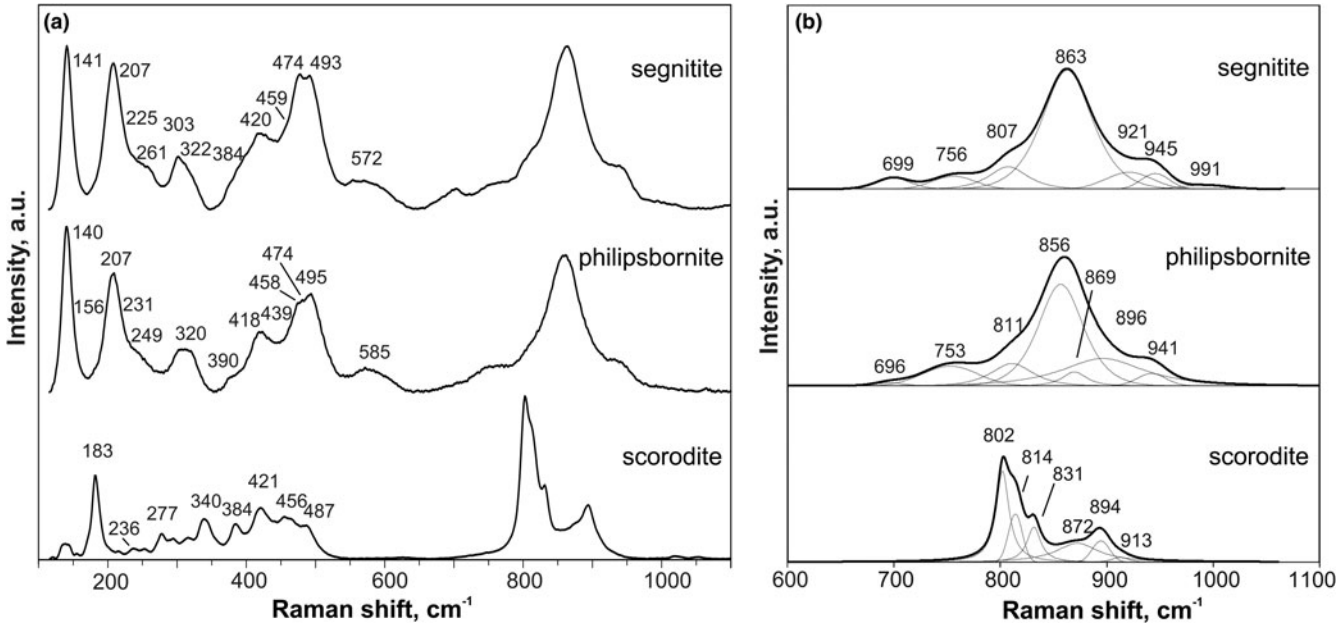

Figure 12. Examples of Raman spectra of (a) segnitite and philipsbornite compared to scorodite in the region of 100–1100 cm^{-1} excited by 532 nm laser. (b) The results of fitting and decomposition in the stretching region.

https://doi.org/10.1180/mgm.2023.75 Published online by Cambridge University Press

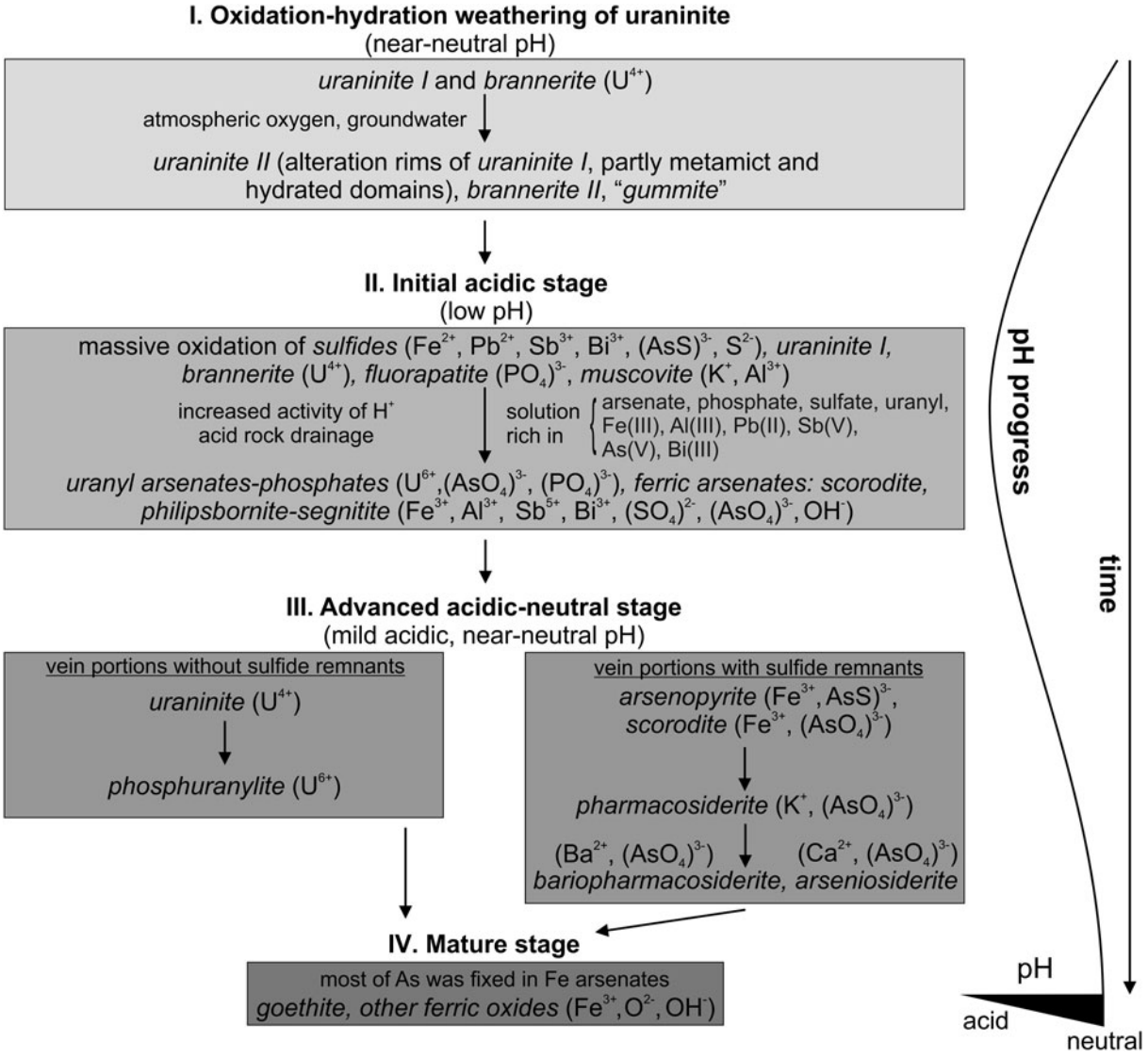

Figure 13. Summary scheme of the oxidation zone main stages.

to adsorb Sb, have negligible concentrations of these elements (Fig. 6b). Antimony and Bi are rather exceptional components of the philipsbornite–segnitite alunite-supergroup mineral phases and suggest unusual conditions during formation from the Sb–Bi precursors (in our case, stibnite, gudmundite, berthierite, tetrahedrite-(Fe), gersdorffite and tintinaite–kobellite). The acidic conditions and sizeable As supply during the initial acidic stage created conditions conducive for the precipitation of the alunite-supergroup mineral phases. Philipsbornite is a stable phase under acidic conditions (pH < 4; Leverett *et al.*, 2003) and segnitite could be synthesised by hydrothermal methods in the pH range 1.0–1.5 (Mills, 2007). Furthermore, Sb-rich segnitite from Black Pine Mine, Montana, USA appears to have formed under oxidising conditions and pH < 2 (Mills *et al.*, 2014). The alunite-supergroup mineral phases removed Sb and Bi from the acidic solutions and locked them up in their crystal structures. Doing so, they depleted the solutions in Sb and Bi to the extent that these elements were not available for the secondary minerals that formed later. Apart from philipsbornite–segnitite, scorodite is also abundant. This mineral, however, does not tolerate Sb in its structure because of the different size and coordination of As^{5+} and Sb^{5+} (Kossoff *et al.*, 2015).

Variations in the uranyl minerals in response to environmental conditions

The formation of the autunite-group minerals conforms to the strongly acidic environment of the initial acidic stage. Uranyl arsenates prevail over phosphates, and both probably precipitate from an aqueous solution rich in uranyl complexes at a high activity of As(V) and comparatively lower activity of P(V). In contrast, the less abundant phosphuranylite was formed under near-neutral conditions once the sulfides vanished and ceased supplying acidity into the weathering fluids (cf. Krivovichev and Plášil, 2013; Plášil, 2014). The change in the assemblages of the uranyl minerals indicates, together with pharmacosiderite–bariopharmacosiderite and arseniosiderite (cf. Drahota and Filippi, 2009 and references therein), the gradual change from strongly acidic to mildly acidic or near-neutral conditions.

https://doi.org/10.1180/mgm.2023.75 Published online by Cambridge University Press

Conclusions

In this work, we investigated weathering of hypogene minerals within the oxidation zone at the Prakovce-Zimná Voda REE–U–Au quartz vein, Gemeric Unit, Western Carpathians, Slovakia. These minerals weather and develop alteration rims or are totally replaced by a variety of supergene phases rich in Fe, As, U, Pb, Sb, Bi, S, P, Ca and Ba. This supergene mineral assemblage represents a typical stable association under the surface conditions of the oxidised zone in the uranium deposits. Uranyl arsenates and minor phosphates of autunite-type group together with scorodite and philipsbornite–segnitite-series minerals formed by oxidising fluids during decomposition and leaching of primary hypogene uraninite, brannerite and base-metal sulfides, such as arsenopyrite, gersdorffite, pyrite, galena, minerals of the stibnite–bismuthinite series and tintinaite–kobellite. A progressive change of pH from acidic to near-neutral due to the gradual consumption of sulfides resulted in the formation of late phosphuranylite, pharmacosiderite and arseniosiderite. Goethite represents the latest hydrous ferric oxide.

Using the μ-XAS technique, we found that the oxidation state of Sb in philipsbornite–segnitite-series minerals is essentially pentavalent, and together with the presence of Fe oxides and arsenates (Fe^{3+}) and uranyl minerals (U^{6+}) suggests oxidative conditions during weathering. Our study also indicates that in the supergene environment in the quartz vein rich in Fe and As, accompanied by elevated concentrations of U, Pb, Sb, Bi, S, P, Ca and Ba at oxidising conditions, various hydrous ferric arsenates are dominant secondary minerals. Uranium was incorporated into uranyl arsenates–phosphates, whereas Sb, Bi and Pb were taken up into philipsbornite–segnitite. Antimony and Bi are rather exceptional within this mineral supergroup and suggest unusual conditions (i.e. very low pH) during their formation. Phosphate binds preferentially with Al whereas arsenate has higher affinity to Fe^{3+} in most of the minerals studied, however, the strongest P–Al and As–Fe synergy is documented in the alunite-supergroup minerals. The source of Fe, As, Pb, Bi, Sb, and S was probably the base-metal sulfides (particularly arsenopyrite and pyrite) and sulfosalts (minerals of the bismuthinite–stibnite and kobellite–tintinaite series), whereas U was released from uraninite and brannerite, P from fluorapatite and Al, K and Ba from muscovite or from feldspars in the host rocks.

Acknowledgements. This work was supported by the Slovak Research and Development Agency under contract Nos. APVV-22-0041 and APVV-22-0092 and VEGA Agency 2/0029/23, 1/0467/20 and 1/0563/22. Analytical laboratories in Banská Bystrica are supported by the European Regional Development Fund through projects ITMS 26220120064 and ITMS 26210120013. We thank P. Konečný and V. Kollárová for providing the EPMA facilities. We are also grateful to Ladislav Novotný for providing parts of the samples (URANPRES).

Competing interests. The authors declare none.

Supplementary material. The supplementary material for this article can be found at https://doi.org/10.1180/mgm.2023.75.

References

Adlakha E.E. and Hattori K. (2015) Compositional variation and timing of aluminum phosphate-sulfate minerals in the basement rocks along the P2 fault and in association with the McArthur River uranium deposit, Athabasca Basin, Saskatchewan, Canada. *American Mineralogist*, **100**, 1386–1399.

Bajaník Š., Ivanička J., Mello J., Reichwalder P., Pristaš J., Snopko L., Vozár J., and Vozárová A. (1984) *Geological map of the Slovenské Rudohorie Mts.—Eastern part, 1: 50 000, 1st ed.* State Geological Institute of D.Štúr, Bratislava, Czechoslovakia [in Slovak].

Bayliss P., Kolitsch U., Nickel E.H. and Pring A. (2010) Alunite supergroup: recommended nomenclature. *Mineralogical Magazine*, **74**, 919–927.

Beaufort D., Patrier P., Laverret E., Bruneton P. and Mondy J. (2005) Clay alteration associated with Proterozoic unconformity-type uranium deposits in the East Alligator Rivers uranium field, Northern Territory, Australia. *Economic Geology*, **100**, 515–536.

Belova L.N. (1975) *Oxidation Zones of Hydrothermal Uranium Deposits*. Moscow, Nedra, pp 1–158 [in Russian].

Belova L.N. (2000) Formation conditions of oxidation zones of uranium deposits and uranium mineral accumulations in the hypergenesis zone. *Geology of Ore Deposits*, **42**, 103–110

Birch W.D., Pring A. and Gatehouse B.M. (1992) Segnitite, $PbFe_3H(AsO_4)_2(OH)_6$, a new mineral in the lusungite group from Broken Hill, New South Wales, Australia. *American Mineralogist*, **77**, 656–659.

Cheng H., Hu Y., Luo J., Xu B. and Zhao J., (2009) Geochemical processes controlling fate and transport of arsenic in acid mine drainage (AMD) and natural systems. *Journal of Hazardous Materials*, **165**, 13–26.

Clark A.M., Couper A.G., Embrez P.G. and Fejer E.E. (1986) Waylandite: new data, from an occurrence in Cornwall, with a note on 'agnesite'. *Mineralogical Magazine*, **50**, 731–733.

Cooper M.A. and Hawthorne F.C. (2012) Refinement of the crystal structure of zoned philipsbornite-hidalgoite from the Tsumeb mine, Namibia, and hydrogen bonding in the $D^{2+}G_3^{3+}(T^{5+}O_4)(TO_3OH)(OH)_6$ alunite structures. *Mineralogical Magazine*, **76**, 839–849.

Culka A., Kindlová H., Drahota P. and Jehlička J. (2016) Raman spectroscopic identification of arsenate minerals in situ at outcrops with handheld (532nm, 785nm) instruments, *Spectrochimica Acta Part A: Molecular and Biomolecular Spectroscopy*, **154**, 193–199.

Das B. (2019) Theoretical study of formation of secondary arsenic minerals: scorodite and pharmacosiderite. *ACS Earth and Space Chemistry*, **3**, 192–201.

Das S. and Hendry M.J. (2011) Application of Raman spectroscopy to identify iron minerals commonly found in mine wastes. *Chemical Geology*, **290**, 101–108.

David J., Jahnsa J., Novák F. and Prachař I. (1990) Philipsbornite from the Sn–W deposit Cínovec in Krušné hory Mts. (Czechoslovakia). *Vestnik Ustredniho Ustavu Geologickeho*, **65**, 367–369.

De Faria D.L.A., Venâncio Silva S. and De Oliveira M.T. (1997) Raman microspectroscopy of some iron oxides and oxyhydroxides. *Journal of Raman Spectroscopy*, **28**, 873–878.

Desborough G.A., Smith K.S., Lowers H.A., Swayze G.A., Hammarstrom J.M., Diehl S.F., Leinz R.W. and Driscoll R.L. (2010) Mineralogical and chemical characteristics of some natural jarosites. *Geochimica et Cosmochimica Acta*, **74**, 1041–1056.

Dill H.G. (2001) The geology of aluminum phosphates and sulphates of the alunite group minerals: a review. *Earth Science Reviews*, **53**, 35–93.

Donát A., Mihaľ F. and Novotný L. (2000) Geological-Exploration Works on the Au in Lower Paleozoic of Spišsko-Gemerské Rudohorie Mts. *Unpublished Report, State Geological Institute of D. Štúr, Bratislava*, pp 1–209 [in Slovak].

Drahota P. and Filippi M. (2009) Secondary As minerals in the environment: a review. *Environment International*, **35**, 1243–1255

Drahota P., Rohovec J., Filippi M., Mihaljevič M., Rychlovský P., Červený V. and Pertold Z. (2009) Mineralogical and geochemical controls on arsenic speciation and mobility under different redox conditions in soil, sediment and water at the Mokrsko-West gold deposit, Czech Republic. *Science of The Total Environment*, **407**, 3372–84.

Dutrizac J.E. and Jambor J.L. (2000) Jarosites and their application in hydrometallurgy. Pp. 405–452 in: *Sulfate Minerals: Crystallography, Geochemistry, and Environmental Significance* (C.N. Alpers, J.L. Jambor and D.K. Nordstrom, editors) Reviews in Mineralogy & Geochemistry, **40**. Mineralogical Society of America and the Geochemical Society, Washington DC.

Ferenc Š., Biroň A., Mikuš M., Spišiak J. and Budzák Š. (2018) Initial replacement stage of primary uranium (U^{IV}) minerals by supergene alteration:

association of uranyl-oxide hydroxy–hydrates and "calciolepersonnite" from the Krátka Dolina Valley (Gemerská Poloma, Gemeric Unit, Western Carpathians, Slovakia). *Journal of Geosciences*, **63**, 277–291.

Ferenc Š., Mikuš T., Kopáčik R., Vlasáč J. and Hoppanová E. (2022) Cu-(U) mineralisation in the copper sandstones at Šafárka occurrence near Novoveská Huta (Spišská Nová Ves), Spišsko-gemerské Rudohorie Mts., Western Carpathians, Gemeric Unit, eastern Slovakia. *Acta Geologica Slovaca*, **14**, 87–101.

Filippi M., Doušová B. and Machovič V. (2007) Arsenic in contaminated soils and anthropogenic deposits at the Mokrsko, Roudný, and Kašperské Hory gold deposits, Bohemian Massif CZ. *Geoderma*, **139**, 154–170.

Frost R.L., Weier M.L., Martens W. and Mills S. (2005) Molecular structure of segnitite: A Raman spectroscopic study. *Journal of Molecular Structure*, **752**, 178–185.

Frost R.L., Bahfenne S., Čejka J., Sejkora J., Plášil J., Palmer S.J., Keeffe E.C. and Němec I. (2011) Dussertite $BaFe^{+3}_3(AsO_4)_2(OH)_5$ – a Raman spectroscopic study of a hydroxy-arsenate mineral. *Journal of Raman Spectroscopy*, **42**, 56–61.

Frost R.L., Xi Y., Pogson R.E. and Scholz R. (2013) A vibrational spectroscopic study of philipsbornite $PbAl_3(AsO_4)_2(OH)_5{\cdot}H_2O$-molecular structural implications and relationship to the crandallite subgroup arsenates. *Spectrochimica Acta Part A: Molecular and Biomolecular Spectroscopy*, **104**, 257–261.

Gaboreau S., Beaufort D., Viellard P. and Patrier P. (2005) Aluminum phosphate-sulfate minerals associated with Proterozoic unconformity-type uranium deposits in the East Alligator River uranium field, Northern Territories, Australia. *The Canadian Mineralogist*, **43**, 813–827.

Gaboreau S., Cuney M., Quirt D., Beaufort D., Patrier P. and Mathieu R. (2007) Significance of aluminum phosphate-sulfate minerals associated with U unconformity-type deposits: The Athabasca basin, Canada. *American Mineralogist*, **92**, 267–280.

Göb S., Gühring J-E, Bau M. and Markl G. (2013) Remobilization of U and REE and the formation of secondary minerals in oxidized U deposits. *American Mineralogist*, **98**, 530–548.

Golebiowska B., Włodek A., Pieczka A., Borkiewicz O. and Polak M (2016) The philipsbornite-segnitite solid-solution series from Rędziny, eastern metamorphic cover of the Karkonosze granite (SW Poland). *Annales Societatis Geologorum Poloniae*, **86**, 73–83.

Herrmann J., Voegelin A, Palatinus L., Mangold S. and Majzlan J. (2018) Secondary Fe–As–Tl mineralization in soils near Buus in the Swiss Jura Mountains. *European Journal of Mineralogy*, **30**, 887–898.

Kloprogge J.T. and Wood B.J. (2017) X-ray Photoelectron Spectroscopic and Raman microscopic investigation of the variscite group minerals: Variscite, strengite, scorodite and mansfieldite. *Spectrochimica Acta Part A: Molecular and Biomolecular Spectroscopy*, **185**, 163–172.

Kobulský J., Gazdačko Ľ. and Grecula P. (2011) Raw materials. Pp. 1–308 in: *Explanations to the geological map of the Spiš-Gemer Ore Mountains* (Grecula P, Kobulský J, editors). The Dionýz Štúr State Geological Institute, Bratislava [in Slovak].

Kohút M., Trubač J., Novotný L., Ackerman L., Demko R., Bartalský B. and Erban V. (2013) Geology and Re–Os molybdenite geochronology of the Kurišková U–Mo deposit (Western Carpathians, Slovakia). *Journal of Geosciences*, **58**, 271–282.

Kolitsch U., Slade P.G., Tiekink E.R.T. and Pring A. (1999) The structure of antimonian dussertite and the role of antimony in oxysalt minerals. *Mineralogical Magazine*, **63**, 17–26.

Kossoff D., Welch M.D. and Hudson-Edwards K.A. (2015) Scorodite precipitation in the presence of antimony. *Chemical Geology*, **406**, 1–9.

Krivovichev S.V. and Plášil J. (2013) Mineralogy and crystallography of uranium. Pp. 15–119 in: *Uranium: From Cradle to Grave* (Burns PC, Sigmon GE, editors). Mineralogical Association of Canada Short Courses, **43**.

Kroumova E., Aroyo M.I., Perez-Mato J.M., Kirov A., Capillas C., Ivantchev S. and Wondratschek H. (2003) Bilbao Crystallographic Server: useful databases and tools for phase transitions studies. *Phase Transitions*, **76**, 155–170.

Lafuente B., Downs R.T., Yang H. and Stone N. (2015) The power of databases: the RRUFF project. Pp. 1–30 in: *Highlights in Mineralogical Crystallography* (Armbruster, T. and Danisi, R.M., editors). De Gruyter, Berlin, Germany.

Lalinská-Voleková B., Majzlan J., Klimko T., Chovan M., Kučerová G., Michňová J., Hovorič R., Göttlicher J. and Steininger R. (2012) Mineralogy of weathering products of Fe–As–Sb mine wastes and soils at several Sb deposits in Slovakia. *The Canadian Mineralogist*, **50**, 481–500.

Lalinská-Voleková B., Majerová H., Kautmanová I., Brachtýr O., Szabóová D., Arendt D., Brčeková J. and Šottník P. (2022) Hydrous ferric oxides (HFO's) precipitated from contaminated waters at several abandoned Sb deposits – Interdisciplinary assessment. *Science of the Total Environment*, **821**, 153248.

Leverett P., McKinnon A.R. and Williams P.A. (2003) Mineralogy of the oxidized zone at the New Cobar ore body. Pp 267–270 in: *Advances in Regolith* (Roach, I.C., editor). CRC LEME Regional Regolith Symposia, Adelaide, Australia.

Majzlan J., Lalinská B., Chovan M., Jurkovič Ľ., Milovská S. and Göttlicher J. (2007) The formation, structure, and ageing of As-rich hydrous ferric oxide at the abandoned Sb deposit Pezinok (Slovakia). *Geochimica et Cosmochimica Acta*, **71**, 4206–4220.

Majzlan J., Lalinská B., Chovan M., Blaß U., Brecht B., Göttlicher J., Steininger R., Hug K., Ziegler S. and Gescher J. (2011) A mineralogical, geochemical, and microbiogical assessment of the antimony- and arsenic-rich neutral mine drainage tailings near Pezinok, Slovakia. *American Mineralogist*, **96**, 1–13.

Majzlan J., Drahota P., Filippi M., Grevel K.-D., Kahl W.-A., Plášil J., Boerio-Goates J. and Woodfield B.F. (2012) Thermodynamic properties of scorodite and parascorodite ($FeAsO_4{\cdot}2H_2O$), kaňkite ($FeAsO_4{\cdot}3.5H_2O$), and $FeAsO_4$. *Hydrometallurgy*, **117–118**, 47–56.

Majzlan J., Haase P., Plášil J. and Dachs E. (2019) Synthesis and stability of some members of the pharmacosiderite group, $AFe_4(OH)_4(AsO_4)_3{\cdot}nH_2O$ (A = K, Na, 0.5Ba, 0.5Sr). *The Canadian Mineralogist*, **57**, 663–675.

Mills S.J. (2007) *The Crystal Chemistry and Geochronology of Minerals From Broken Hill*. Unpublished Ph.D. thesis, University of Melbourne, Australia.

Mills S.J., Kampf A.R., Raudsepp M. and Birch W.D. (2010) The crystal structure of waylandite from Wheal Remfry, Cornwall, United Kingdom. *Mineralogy and Petrology*, **100**, 249–253.

Mills S.J., Etschmann B., Kampf A.R., Poirier G. and Newville M. (2014) Sb^{5+} and Sb^{3+} substitution in segnitite: A new sink for As and Sb in the environment and implications for acid mine drainage. *American Mineralogist*, **99**, 1355–1359.

Moura M.A., Botelho N.F. and Carvalho de Mendonça F. (2007) The indium-rich sulfides and rare arsenates of the Sn-In-mineralized Mangabeira A-type granite, Central Brazil. *The Canadian Mineralogist*, **45**, 485–496.

Müller K., Ciminelli V.S.T., Dantas M.S.S. and Willscher S. (2010) A comparative study of As(III) and As(V) in aqueous solutions and adsorbed on iron oxy-hydroxides by Raman spectroscopy. *Water Research*, **44**, 5660–5672.

Myneni S.C.B., Traina S.J., Waychunas G.A. and Logan T.J. (1998) Experimental and theoretical vibrational spectroscopic evaluation of arsenate coordination in aqueous solutions, solids, and at mineral-water interfaces. *Geochimica Cosmochimica Acta*, **62**, 3285–3300.

Novotný L. and Čížek P. (1979) New occurrence of uranium– gold mineralization to the south of Prakovce in Spišsko-Gemerské Rudohorie Mts. *Mineralia Slovaca*, **11**, 188–190 [in Slovak].

Novotný L., Háber M., Križáni I., Rojkovič I. and Mihaľ F. (1999) Gold in the Early Paleozoic rocks in the central part of the Spišsko-Gemerské Rudohorie Mts. *Mineralia Slovaca*, **31**, 211–216 [in Slovak].

Ondrejka M., Uher P., Ferenc Š., Majzlan J., Pollok K., Mikuš T., Milovská S., Molnárová A., Škoda R., Kopáčik R., Kurylo S. and Bačík P. (2023a) Monazite-(Gd), a new Gd-dominant mineral of the monazite group from the Zimná Voda REE–U–Au quartz vein, Prakovce, Western Carpathians, Slovakia. *Mineralogical Magazine*, **87**, 568–574.

Ondrejka M., Uher P., Ferenc Š., Milovská S., Mikuš T., Molnárová A., Škoda R., Kopáčik R. and Bačík P. (2023b) Gadolinium-dominant monazite and xenotime: Selective hydrothermal enrichment of middle REE during low-temperature alteration of uraninite, brannerite, and fluorapatite (the Zimná Voda REE-U-Au quartz vein, Western Carpathians, Slovakia). *American Mineralogist*, **108**, 754–768.

Paikaray S. (2015) Arsenic geochemistry of acid mine drainage. *Mine Water and the Environment*, **34**, 181–196.

Paktunc D., Foster A., Heald S. and Laflamme G. (2004) Speciation and characterization of arsenic in gold ores and cyanidation tailings using X-ray absorption spectroscopy. *Geochimica et Cosmochimica Acta*, 68, 969–83.

Paktunc D., Majzlan J., Huang A., Thibault Y., Johnson M. and White M.A. (2015) Synthesis, characterization, and thermodynamics of arsenates

https://doi.org/10.1180/mgm.2023.75 Published online by Cambridge University Press

forming in the Ca-Fe(III)-As(V)-NO3 system: Implications for the stability of Ca-Fe arsenates. *American Mineralogist*, **100**, 1803–1820.

Pekov I.V., Khanin D.A., Yapaskurt V.O., Pakunova A.V. and Ekimenkova I.A. (2016) Minerals of the beudantite–segnitite series from the oxidation zone of the Berezovskoe gold deposit, Middle Urals: chemical variations, behavior of admixtures, and antimonian varieties. *Geology of Ore Deposits*, **58**, 600–611.

Plašienka D., Grecula P., Putiš M., Kováč M. and Hovorka D. (1997) Evolution and structure of the Western Carpathians: an overview. Pp 1–24i in: *Geological Evolution of the Western Carpathians* (P. Grecula, D. Hovorka and M. Putiš, editors). Mineralia Slovaca Monograph, Bratislava.

Plášil J. (2014) Oxidation–hydration weathering of uraninite: the current state-of-knowledge, *Journal of Geosciences*, **59**, 99–114.

Rattray K.J., Taylor M.R., Bevan D.J.M. and Pring A. (1996) Compositional segregation and solid solution in the lead-dominant alunite-type minerals from Broken Hill, N.S.W. *Mineralogical Magazine*, **60**, 779–785.

Ravel B. and Newville M. (2005) ATHENA, ARTEMIS, HEPHAESTUS: data analysis for X-ray absorption spectroscopy using IFEFFIT. *Journal of Synchrotron Radiation*, **12**, 537–541.

Rojkovič I. (1997) *Uranium Mineralization in Slovakia*. Comenius University, Bratislava, pp. 1–117.

Rojkovič I. and Novotný L. (1993) Uranium mineralization in Gemericum. *Mineralia Slovaca*, **25**, 368–370 [in Slovak].

Rojkovič I., Háber M. and Novotný L. (1997) U–Au–Co– Bi–REE mineralization in the Gemeric Unit (Western Carpathians, Slovakia). *Geologica Carpathica*, **48**, 303–313

Scharm B., Scharmová M. and Kundrát M. (1994) Crandalite group minerals in the uranium ore district of Northern Bohemia (Czech Republic). *Věstník Českého Geologického Ústavu*, **69**, 79–85.

Sejkora J., Ondruš P., Fikar M., Veselovský F., Mach Z., Gabašová A., Škoda R. and Beran P. (2006) Supergene minerals at the Huber stock and Schnod stock deposits, Krásno ore district, the Slavkovský les area, Czech Republic. *Journal of Czech Geological Society*, **51**, 57–101.

Sejkora J., Škovíra J., Čejka J. and Plášil J (2009) Cu-rich members of the beudantite–segnitite series from the Krupka ore district, the Krušné hory Mountains, Czech Republic. *Journal of Geosciences*, **54**, 355–371.

Sejkora J., Plášil J., Císařová I., Škoda R., Hloušek J., Veselovský F. and Jebavá I. (2011) Interesting supergene Pb-rich mineral association from the Rovnost mining field, Jáchymov (St. Joachimsthal), Czech Republic. *Journal of Geosciences*, **56**, 257–271.

Sejkora J., Pauliš P., Urban M., Dolníček Z., Ulmanová J. and Pour O. (2021) Mineralogy of quartz veins of the tin deposit Hřebečná near Abertamy in Krušné hory Mountains (Czech Republic). *Bulletin Mineralogie Petrologie* **29**, 131–163 [in Czech with English abstract].

Števko M., Uher P., Ondrejka M., Ozdín D. and Bačík P. (2014) Quartz–apatite– REE phosphates–uraninite vein mineralization near Čučma (eastern Slovakia): A product of early Alpine hydrothermal activity in the Gemeric Superunit, Western Carpathians. *Journal of Geosciences*, **59**, 209–222.

Števko M., Sejkora J. and Malíková R. (2016) New data on supergene minerals from the Rainer mining field, Ľubietová - Podlipa deposit (Slovak Republic). *Bulletin Mineralogie Petrologie* **24**, 1–12 [in Slovak with English abstract].

Uehara S. and Shirose Y. (2013) Namibite and hechtsbergite from the Nagatare mine, Fukuoka Prefecture, Japan. *Journal of Mineralogical and Petrological Sciences*, **108**, 105–110.

Van Wambeke L. (1975) La zaïrite, un nouveau minéral appartenant à la série de la crandallite. In: *Bulletin de la Société française de Minéralogie et de Cristallographie*, **98**, 351–353 [in French].

Varček C. (1977) Some rare mineralization types in the Spišsko-Gemerské Rudohorie Mts. Pp. 93–99 in: *Ore-Forming Processes in the Western Carpathians* (Háber M., editor). Universitas Comeniana, Bratislava [in Slovak].

Villaseñor G., Catlos E.J., Broska I., Kohút M., Hraško Ľ., Aguilera K., Etzel T.M., Kyle R. and Stockli D.F. (2021) Evidence for widespread mid-Permian magmatic activity related to rifting following the Variscan orogeny (Western Carpathians). *Lithos*, **390–391**, 106083.

Von Knorring O. and Mrose M.E. (1963) Westgrenite [= bismutomicrolite] and waylandite, two new bismuth minerals from Uganda. *Geological Society of America Special Paper*, **73**, 256A.

Walker S.R., Jamieson H.E., Lanzirotti A., Andrade C.F. and Hall G.E.M. (2005). The speciation of arsenic in iron oxides in mine wastes from the Giant gold mine, NWT: application of synchrotron micro-XRD and micro-XANES at the grain scale. *The Canadian Mineralogist* **43**, 1205–1224.

Warr L.N. (2021) IMA–CNMNC approved mineral symbols. *Mineralogical Magazine*, **85**, 291–320.

Welch S.A., Christy A.G., Kirste D., Beavis S.G. and Beavis F. (2007) Jarosite dissolution I − trace cation flux in acid sulfate soils. *Chemical Geology*, **245**, 183–197.

Welch S.A., Kirste D., Christy A.G., Beavis F.R. and Beavis S.G. (2008) Jarosite dissolution II − reaction kinetics, stoichiometry and acid flux. *Chemical Geology*, **254**, 73–86.

Welch S.A., Christy A.G., Isaacson L. and Kirste D. (2009) Mineralogical control of rare earth elements in acid sulfate soils. *Geochimica et Cosmochimica Acta*, **73**, 44–64.

Zhang J., Liang X., Wang F., Wang H., Fan Y., Ba T. and Meng X. (2023) CorelKit: An Extensible CorelDraw VBA Program for Geoscience Drawing. *Journal of Earth Science*, **34**, 735–757.

https://doi.org/10.1180/mgm.2023.75 Published online by Cambridge University Press